Characterization and Theoretical Study of

Mid-infrared Quantum Cascade Lasers

By

Xiaoliang He

A thesis

presented to the University of Waterloo

in fulfillment of the

thesis requirement for the degree of

Master of Applied Science

in

Electrical and Computer Engineering (Nanotechnology)

Waterloo, Ontario, Canada, 2019

Author's Declaration

I hereby declare that I am the sole author of this thesis. This is a true copy of the thesis, including any required final revisions, as accepted by my examiners.

I understand that my thesis may be electronically available to the public.

Abstract

The technology and performance of quantum cascade lasers has rapidly developed since it was firstly unveiled in 1994 [1]. This type of laser has a feasible design, micro meter size and potential for emission of long wavelength (mid-infrared to far-infrared); hence, it can be useful for multiple applications. Because of the lack of light source in the mid-infrared range (wavelengths of 3-30 μm), the mid-infrared quantum cascade lasers with high quality radiation are playing important roles in several research fields such as chemical and bio-chemical spectroscopy, free space gas sensing [2] and communication [3].

This work reports the design, fabrication and characterization of the mid-infrared quantum cascade lasers. The theoretical part of this thesis presents the simulation methods of the mid-infrared quantum cascade lasers. The modeling results include the Schrödinger equation solver, quantum transition simulation, and the optical property calculation, among others. The experimental part reports the whole process of the mid-infrared quantum cascade lasers completed at the University of Waterloo.

In summary, the design, optimization, fabrication and characterization of the mid-infrared quantum cascade lasers is verified and improved.

Acknowledgements

I would like to thank my supervisor Dr. Dayan Ban for his encouragement, patience and guidance throughout the duration of my master program. I must thank him for helping me complete the academic project.

I would like to appreciate the collaborators of this project. I would like to thank Prof. Zbigniew Wasilewski for providing the technique of material growth. I would like to thank Dr. Seyed Ghasem Razavipour for theoretical support. I also want to thank Siyi Wang for fabricating most of the devices.

I also would like to express my thanks to my groupmates Dr. Chao Xu, Boyu Wen, Xueren Wang and Yue Zhuo for the helpful discussions and advices.

Finally, I must acknowledge my parents, who give me all aspects of support.

Table of contents

List of figures

List of Tables

Chapter 1

Introduction

1.1 Mid-infrared Radiation

Infrared radiation is an electromagnetic radiation with wavelengths longer than visible light. Normally, the infrared radiation is divided to three spectral regions: near, mid and far-infrared. The region of mid infrared light consist of wavelengths in the range of 3-30 ~µm and photon energy of 40-400 meV, as in Figure 1.1. The spectral region of the mid-infrared is an area of interest to a number of research fields, as most molecules show a characteristic transition in this domain of energy. This makes the mid infrared light a univocal source of characterizing and identifying some molecules. In two of the windows (3-5 and 8-13 µm) within the mid infrared domain, the atmosphere is almost transparent. These two windows may provide a potential of long distance propagation. Furthermore, some reports of large field gas tracing have also shown the importance of mid infrared light [4].
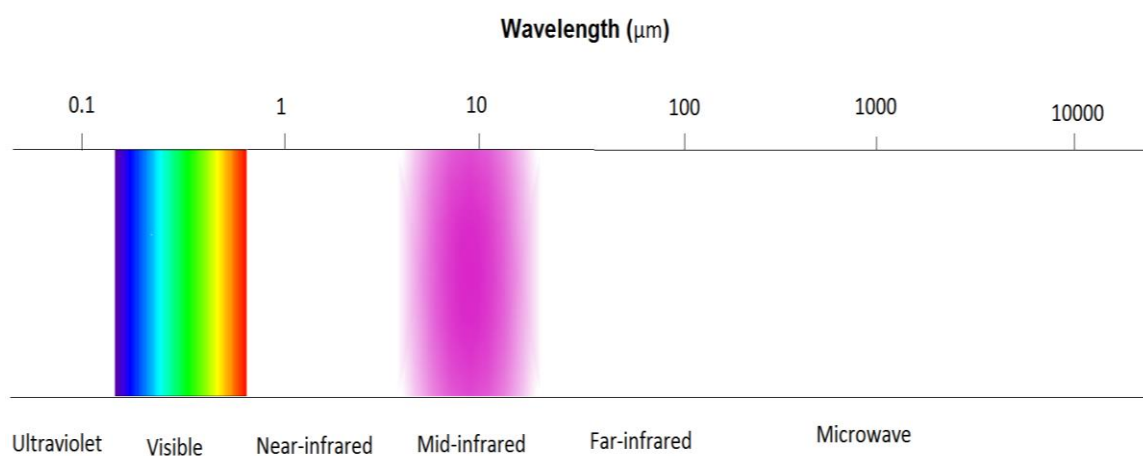
Figure 1.1: Spectrum showing the location of mid-infrared radiation.

1.2 Mid-infrared Source

Black body radiation follows Planck's law of black body radiation

$$B_\nu(T) = \frac{2h\nu^3}{c^2} \frac{1}{e^{\frac{h\nu}{kT}} - 1} \tag{1.1}$$

According to the formula, an object at room temperature (~295 K) emits electromagnetic wave in the range of the mid infrared. The earth itself is a source of mid-infrared radiation, just like everything at room temperature. Most research in the related fields of science and technology, functional and adjustable light source is required. In the past decades, numerous researches were conducted to investigate sources for producing high quality mid-infrared radiation.
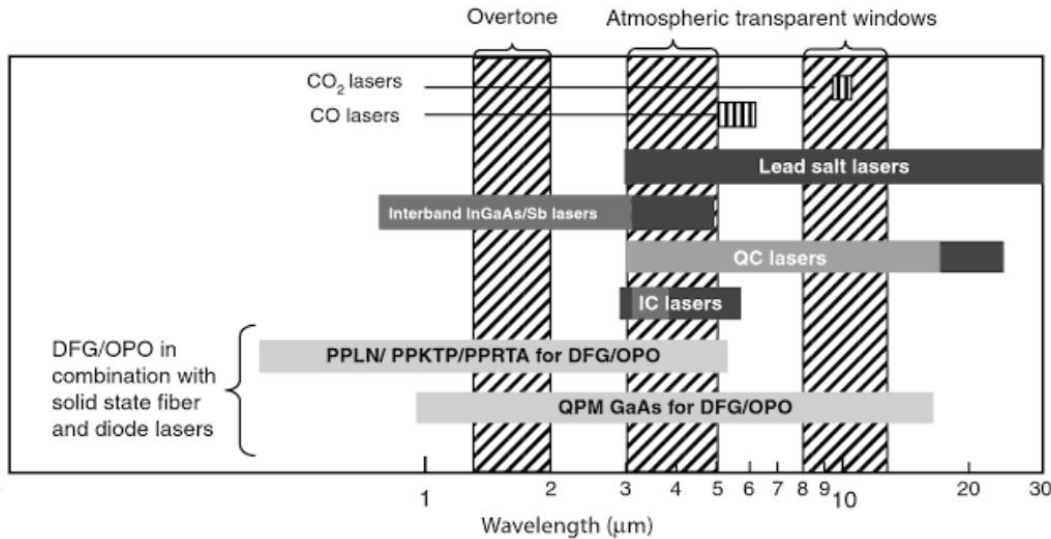
Figure 1.2: Wavelength coverage of the different light sources in infrared range [1].

Figure 1.2 compares the wavelength coverage of the different sources in the near- and mid- infrared regions. Because of the width of the energy gaps, most of the direct light sources in the long wavelength range (not based on DFG or other techniques) are based on the intersubband transition in semiconductors instead of the interband transition. The wavelengths of CO and CO2 gas lasers are fixed to several transition lines. Although the non-linear down conversion technique may change the frequency of gas lasers, it is however, relatively complex and expensive. Besides the quantum cascade lasers, IV-VI lead salt semiconductor lasers can also cover a wide frequency range, but this kind of laser is always limited in terms of reliability and working situation. Based on the best reports published, the quantum cascade lasers

have achieved room temperature operation and wide wavelength coverage (3-16 μm) with high power (above watt).

1.3 Interband and Intersubband

Electron transition in artificial structures is an important topic in semiconductor physics. Interband transition has been proven to be a good source of photon emission as indeed most of the commercial LED products are based on interband transition. Another type of electron transition that has not been well investigated is the intersubband transition. In contrast to the interband transition, intersubband transition occurs in between states in the conduction band. The energy of intersubband transition is typically lower than that of interband transition. Thus, the intersubband transition is a potential approach to achieve mid-infrared or far-infrared radiation. The first laser based on intersubband transition is the quantum cascade laser, developed in 1994 [5]. Since then, this device has been investigated by a number of groups around the world, and, research on QCL is still very active [6].

A hetero-junction is the interface between two different materials. The combination of two semiconductor materials with different band gaps offers the possibility to engineer the band structure. As shown in Figure 1.3, the band gap of the barrier material is larger than that of the well material. Thus, in the conduction band, a quantum well is produced to trap electrons. With the help of molecular beam epitaxy, we have a $GaAs/Al_xGa_{1-x}As$ and $InAs/AlSb$ hetero-structure with very good quality. The design of mid-infrared quantum cascade lasers is based on the energy structure of these hetero material epitaxy layers.
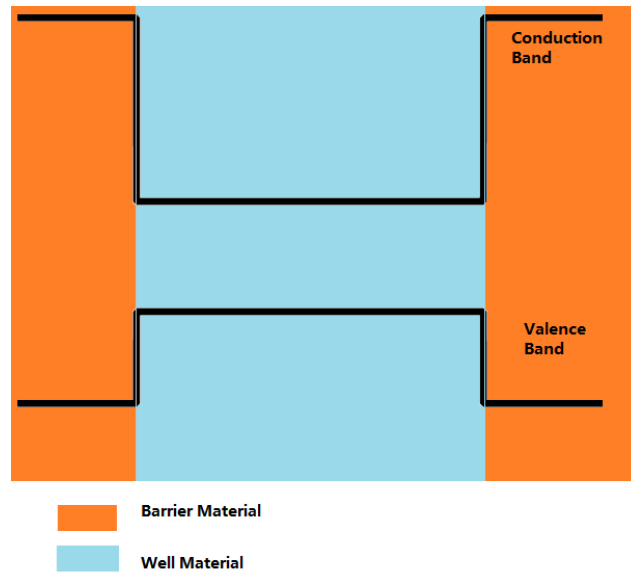
Figure 1.3: Energy structure of an heterostructure. Potential barriers are formed due to the energy gaps of the two materials.

An interband transition occurs between the two states located on the conduction and valence band, Figure 1.4. These two energy states are separated by a band gap mainly defined by the type of material. Thus the lower limit of the transition energy is the band gap of the quantum well material. On the other hand, an intersubband transition happens between two states both in the conduction band. The energy separation of these two states is the difference of the confinement energies of the electronic states in the quantum well. For this reason, the energy will tend to zero as the well's width increases. As a result, quantum cascade lasers show a significant advantage of long wavelength light radiation.
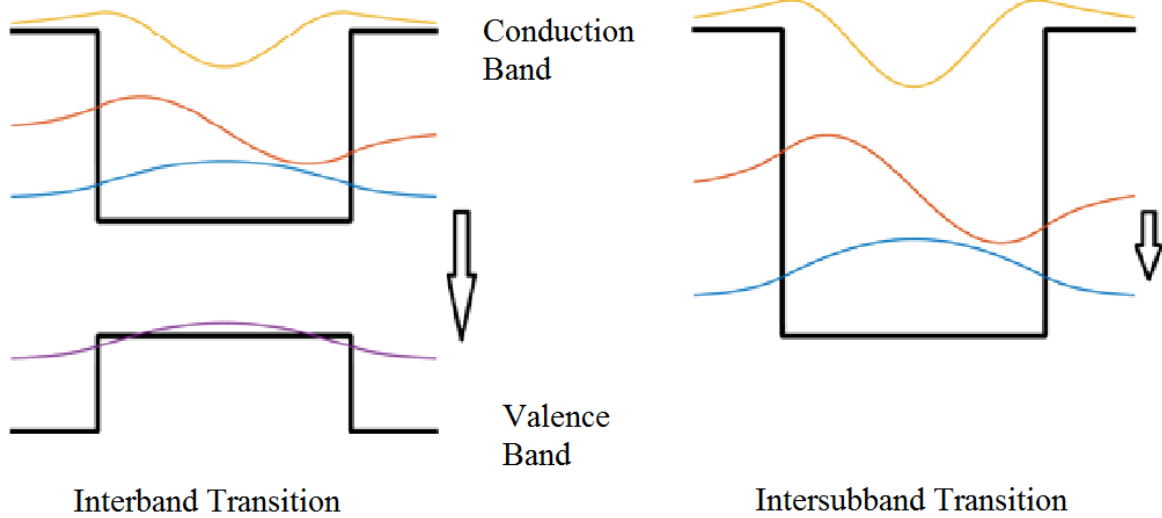
Figure 1.4: Schematic of interband and intersubband transitions.

Considering the E-k property of a semiconductor material in Figure 1.5, it shows that the interband states are truly separated by an energy gap. In contrast, the dispersions of energy are similar for the states in the conduction band. Any elastic and inelastic scattering with suitable momentum or energy may cause the intersubband transition. The lifetime of the electrons is therefore rather short, typically around a picosecond. Quantum cascade lasers are supposed to be well designed to control both the electron distribution and the radiative efficiency.
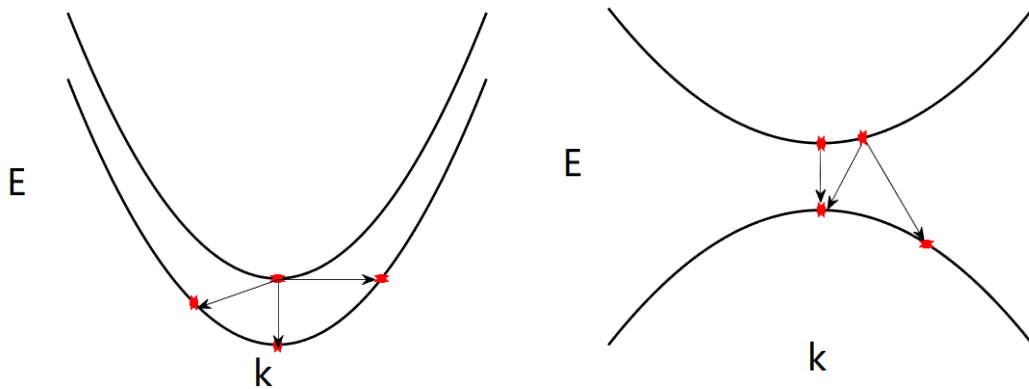
Figure 1.5: Energy-momentum (E-k) diagrams of intersubband (left) and interband (right) transitions.

1.4 Quantum Cascade Lasers

The quantum cascade laser was proposed and achieved by Bell Lab in 1994 [5]. It is a type of laser based on intersubband transition. This great innovation provides us with a way to achieve lasers of long wavelength. In the structure of QCLs, the lasing transition occurs in a repeated stack of semiconductor materials. The layered semiconductor forms multiple quantum wells, in which electrons are trapped. Once a bias electrical field is applied to the structure, the flow of the electrons then provides the energy of the radiation. By carefully designing the quantum structure, a population inversion may occur between specific states, Figure 1.6 shows the energy structure of a MIR QCL. The population inversion is the fundamental condition of the lasing operation.
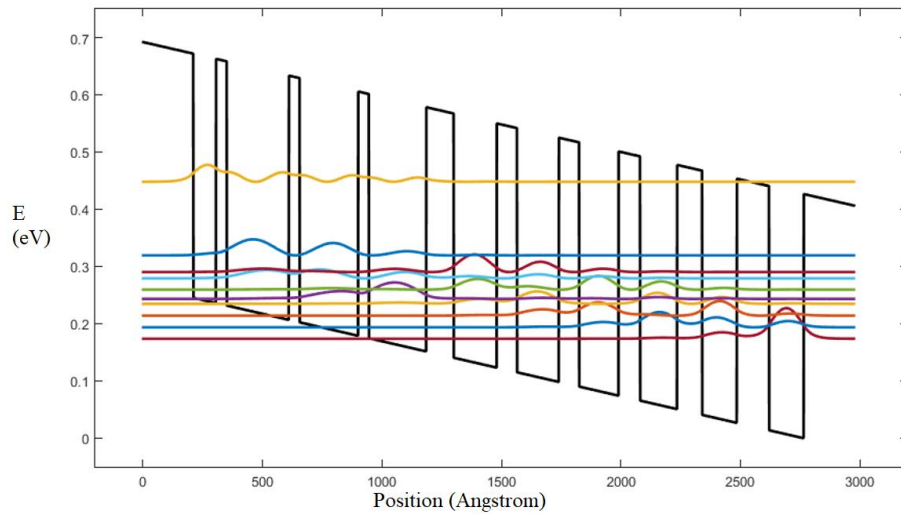
Figure 1.6: Energy structure and wave functions of a mid-infrared quantum cascade laser. Only the conduction band is shown here.

In Figure 1.6, the allowed energy states and wave functions are calculated using the Schrödinger equation solver program. The curves with different colors indicate different energy states and wave functions. The black line indicates the structure of the conduction band.

1.5 Material System
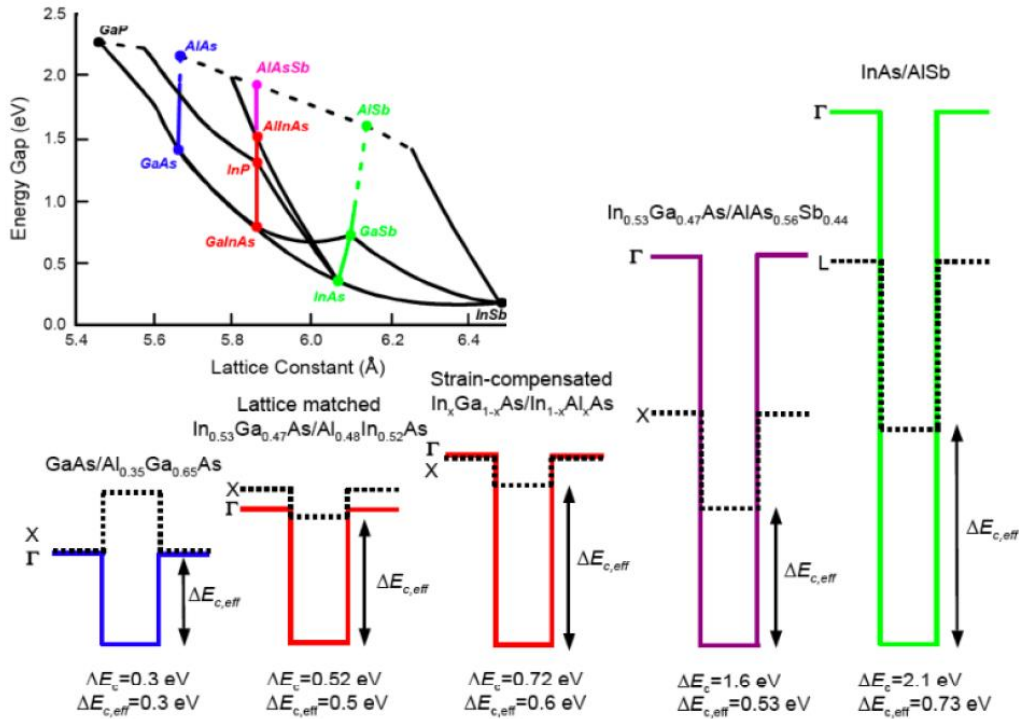
Figure 1.7: Energy gap (barrier height) of various types of semiconductor materials. [7]

Many III-V semiconductor materials could be applied to realize the mid-infrared quantum cascade lasers as shown in Figure 1.7. Several material systems are widely used, these include: GaInAs/AlInAs based on InP substrates [8], GaAs/AlGaAs on GaAs substrates [9], InGaAs/GaAsSb on InP substrates [10], AlSb/InAs on InAs substrates [11], and so on. In this work, the mid-infrared quantum cascade lasers are realized with two material systems: GaAs/AlGaAs on GaAs and AlSb/InAs on InAs.

Taking GaAs/AlGaAs as an example, the energy gap of the GaAs material is 1.424 eV (corresponding to a wavelength of 870 nm). The effective mass of the Γ valley is 0.063 m_0 (electron rest mass). As can be seen in Figure 1.7, the lattice constants of GaAs and AlAs are almost the same (5.6533 and 5.6611 µm). As a result, the lattice mismatch in this material system (GaAs/Al$_x$Ga$_{1-x}$As) is fairly small, theoretically it is <0.1%. The property of the material provides the potential to adjust and improve the performance of the lasers. Furthermore, the molecular beam epitaxy (MBE) growth technique of GaAs is well developed [12]. In summary, the high quality of the AlGaAs/GaAs superlattice makes the proposed quantum design achievable.

In terms of profile, Figure 1.8 depicts the band diagram of AlxGa1-xAs. With a smaller x (x<45%), AlxGa1-xAs has a direct band gap (the Γ valley is the lowest point of the conduction band). With larger x (x>45%), the band gap becomes indirect. To ensure the quality of the optical transition, the direct band gap materials are preferred for an optical device. According to a previous report [13], the structure with higher fraction of Al is desired to ensure better confinement of electrons. Increasing the content of Al is a method that improves the temperature performance. Figure 1.9 shows the transitions of the losses and the optical emissions. The higher quantum barriers caused by the higher fraction of Al helps the superlattice to trap more electrons in the bottom of the quantum wells. This effect significantly reduces the loss carriers to the continuous band and increases the maximum operating temperature. Thus, for the reported 9 μm mid infrared quantum cascade lasers, $Al_{0.45}Ga_{0.55}As$/GaAs on GaAs substrate is selected as the core materials.

x<0.45   x>0.45
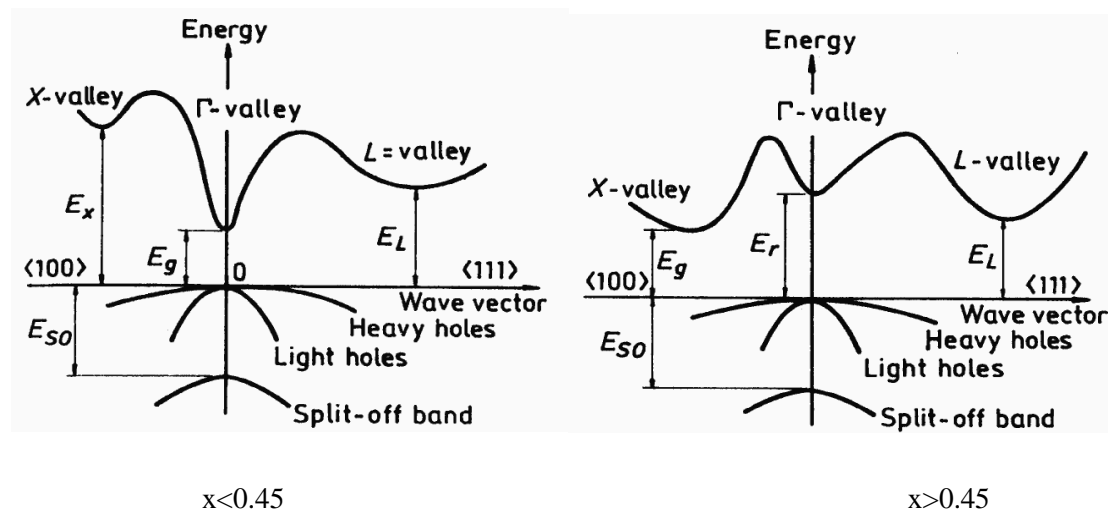
Figure 1.8: E-k diagram of $Al_xGa_{1-x}As$/GaAs material under the condition of x<0.45 and x>0.45. [14]
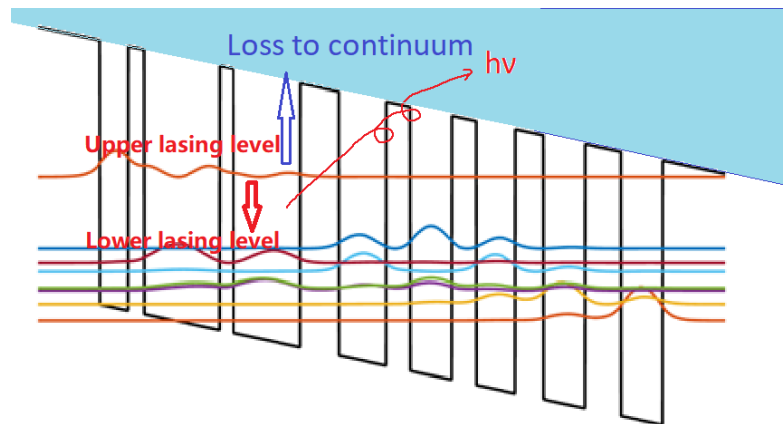
Figure 1.9: Schematic of the transitions of loss and photons.

1.6 Mid-infrared Quantum Cascade Laser Processing

A well-designed hetero-structure is crucial for a mid-infrared quantum cascade laser, as a well-defined energy states can only be obtained in a precise superlattice. Any mismatch or dislocation of the materials may damage the performance of the lasers. The energy diagram of material is highly relative to the crystalline property, so a high quality crystalline structure is required in the growth process of mid-infrared quantum cascade lasers. Since the layers are very thin (even one or two monolayers), the growth rate is supposed to be accurately controlled as well. Ideally, a high quality mid-infrared quantum cascade laser is expected to have an area in the order of 0.01 mm^2 without any crystalline defects, and the thickness of each layer is supposed to be well-controlled in the order of Angstrom. Compared with the traditional semiconductor lasers, the mid-infrared quantum cascade lasers are deeply reliant on the growth technologies. Two types of techniques are available for QCL growth, molecular beam epitaxy (MBE) and metalorganic vapor phase epitaxy (MOCVD) [1].

Most of the mid-infrared quantum cascade reported in this work were grown through Molecular Beam Epitaxy by the research group at the University of Waterloo. MBE is a trusted and reliable technique with tight control of growth rate. Many QCLs have been reported to have being grown via MBE technique [6]. An MBE system consist of a thermal evaporator as the core part, the vacuum chamber which ensure a low base pressure ($\sim 10^{-11}$ mbar) environment, and the ultra-pure elementary substances sealed and heated in different cells. During the growth, gaseous elements may react with each other and form thin films on the wafer. For example, gallium gas and arsenic gas tend to form single-crystal gallium arsenide layers. Typically, the reflection high-energy electron diffraction (RHEED) system can be used in the MBE chamber to monitor the growth rate in-situ. This outstanding accuracy (in the order of Angstrom) of the MBE growth is instrumental to the development of intersubband devices, such as QCLs.

After growing the layered semiconductor materials, the fabrication processes were completed in the clean room of Quantum NanoFab at the University of Waterloo. A brief schematic of the fabrication processes is shown in Fig 1.10. It includes: Photo lithography, focused ion beam etching, chemical coating and etching. The epitaxial layers are fabricated to be ridges. The gold coated anode and cathode are located on the top and bottom surface of the wafers. Normally, silicon nitride is used as the insulating layer to isolate each ridge and reduce the optical loss.
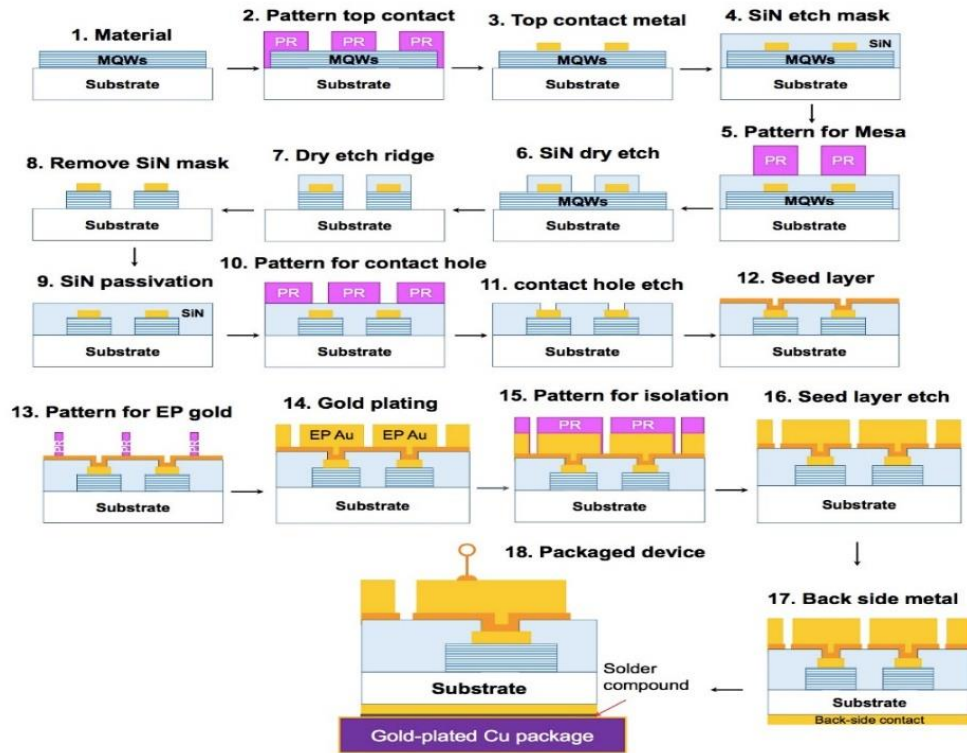
Figure 1.10: Block diagram of the processes for fabricating mid-infrared quantum cascade lasers. [15]

Before sending for measurement, the fabricated devices are mounted on a self-crafted gold coated copper holder. The indium solder under the devices provides the perfect thermal conductivity that accommodates the thermal expansion mismatch of the devices and the metal holder. Furthermore, 15-μm-wide gold wires are connected between the electrodes on the devices and the outside circuit using the wire bonding machine.

1.7 Thesis Overview

The objective of this work is to develop mid-infrared quantum cascade lasers (MIR QCLs) with radiation wavelengths of 3.5 μm and 9 μm. All the devices were grown, fabricated and tested at the University of Waterloo. The author mainly focuses on testing and analysis of the devices' performance. The growing and fabrication processes are completed by other co-workers. The performance of the lasers were measured using the system reported in this work.

The rest of this thesis is organized as follows. Chapter 2 presents the physics background of mid-infrared quantum cascade lasers. Based on the quantum structure of the heterojunction, the transfer matrix method is applied to resolve the energy states and the wave functions. The calculation methods of the scattering mechanisms are introduced based on the previous literature. The transition situation is modeled with the rate equation. The contribution of the electron distribution is also considered as Hartree potential.

The main part of Chapter 3 explains how the experimental setups were built. The chapter introduces the setups for light-current-voltage measurement, spectrum, beam pattern, and the temperature controlling system in detail. All the systems are modified for different devices and statuses. The calibration method is also discussed in this chapter.

The experimental results are introduced in Chapter 4. The performances of different types of MIR QCLs are reported in this chapter. The history of the improvement processes of the mid-infrared quantum cascade lasers, disk and ridge shaped, 3.5 μm and 9 μm lasers are characterized. The 3.5 μm devices show good performances at a temperature up to about 350 K in pulse mode, and the 9 μm lasers are able to emit light at a temperature of up to 250 K. The other results, such as spectrum analysis, also gave additional information about the devices. The mid-infrared quantum cascade lasers are deeply characterized under various conditions.

Chapter 5 comprises the discussion and conclusion of the study, based on the theoretical and experimental results.

Chapter 2

Theoretical Analysis

In this chapter, the theoretical simulation of the mid-infrared quantum cascade lasers is introduced. The first step consist of analyzing the energy structure of the cascaded heterostructure. According to the potential energy in each period, the transfer matrix method could be applied as the Schrödinger equation solver to calculate the eigen states. Thereafter, the transition time among the states can be obtained based on different scattering mechanisms. With the calculated transition time, the carrier distribution could be calculated using the rate equations. After the rate equation calculation, the carrier distribution is the base of optical and electrical feature simulation. Additionally, several effects, such as the nonparabolicity and Hartree potential, are added to this calculation to improve the accuracy. By comparing the simulated and experimental results, the performance of the laser devices can be verified and predicted.

2.1 Transfer Matrix Method (TMM)

To simulate the performance of a mid-infrared quantum cascade laser, it is first necessary to know the wave function of different energy states. Here, a method called transfer matrix is used to solve the Schrödinger equation. This equation is a useful tool for analyzing quantum systems. Considering the quantum wells in the semiconductor hetero structure, the shape of the conduction band edge is a square potential well for electrons. Based on the time independent Schrödinger equation for a one dimensional system:

$$-\frac{\hbar}{2m}\frac{\partial^2}{\partial z^2}\psi(z) + V(z)\psi(z) = E\psi(z) \qquad (2.1)$$

Where z is the position

Ψ is the wave function

V is the potential energy

E is the total energy

In the past century, many mathematical methods have been developed to numerically solve the Schrödinger equation (2.1), these includes the finite difference method (FDM), quantum Monte Carlo method, variational method, and transfer matrix method, among others.

The transfer matrix method is the most widely used for solving the Schrödinger equation in layered materials. Based on the Schrödinger equation, the wave function can be written as

In quantum wells

$$\psi_w = A\exp(ik_w z) + B\exp(-ik_w z) \tag{2.2}$$

In quantum barriers

$$\psi_b = C\exp(ik_b z) + D\exp(-ik_b z) \tag{2.3}$$

Where

$$k_w = \sqrt{\frac{2m_w^*}{\hbar^2}E} \qquad\qquad k_b = \sqrt{\frac{2m_b^*}{\hbar^2}(E-V)}$$
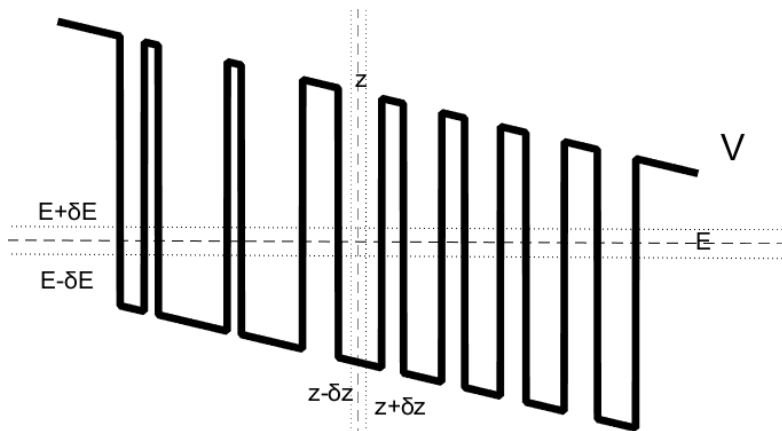
Figure 2.1: The potential structure of a mid-infrared quantum cascade laser and how the region is divided into tiny blocks.

Considering a period of the quantum structure of a MIR QCL, the slope potential energy of the quantum wells and barriers is caused by the external bias voltage. To analyze the energy states inside, the zone is separated into tiny pieces. As shown above in Figure 2.1, the separation is δz in the space domain and δE

in the energy domain. Based on the normal expression of the wave function, the relationship of the wave function is obtained at z-δz, z and z+δz.

For the point x within the small area from z-δz to z+δz. (z-δz<x<z+δz)

$$\psi(x) = A_z \exp\big(ik_z(x - z)\big) + B_z \exp(-ik_z(x - z)) \tag{2.4}$$

$$k_z = \sqrt{\frac{2m_z^*}{\hbar^2}(E - V(z))}$$

If the matrix is used to express the wave function in [16]

$$\begin{bmatrix} A_z \\ B_z \end{bmatrix}$$

Another parameter is obtained [16]

$$P_{z(z+\delta z)} = \frac{m_z^* k_{z+\delta z}}{m_{z+\delta z}^* k_z} \tag{2.5}$$

The relationship of the wave function at z and z+δz can be obtained as

$$\begin{bmatrix} A_{z+\delta z} \\ B_{z+\delta z} \end{bmatrix} = F_{(z+\delta z)z} \begin{bmatrix} A_z \\ B_z \end{bmatrix} \tag{2.6}$$

where

$$F_{(z+\delta z)z} = \frac{1}{2}\begin{bmatrix} \big(1 + P_{(z+\delta z)z}\big)\exp(ik_{z+\delta z}\delta z) & \big(1 - P_{(z+\delta z)z}\big)\exp(ik_{z+\delta z}\delta z) \\ \big(1 - P_{(z+\delta z)z}\big)\exp(-ik_{z+\delta z}\delta z) & \big(1 + P_{(z+\delta z)z}\big)\exp(-ik_{z+\delta z}\delta z) \end{bmatrix} \tag{2.7}$$

In the whole period, the transfer matrix is defined as

$$T_{z_N z_0} = \prod_{j=0}^{N-1} F_{z_j} \tag{2.8}$$

If the system satisfies the box boundary condition (BBC), then the wave function at the side boundaries is supposed to satisfy the rule

$$\psi(z \sim z_0) = B_{z_0} \exp\big(-ik_{z_0}(z - z_0)\big) \tag{2.9}$$

$$\psi(z \sim z_N) = A_{z_N} \exp(ik_{z_N}(z - z_N)) \tag{2.10}$$

which equals to

$$\begin{bmatrix} A_{z_N} \\ 0 \end{bmatrix} = T_{z_N z_0} \begin{bmatrix} 0 \\ B_{z_0} \end{bmatrix} \tag{2.11}$$

Consider the four elements in matrix T

$$T_{z_N z_0} = \begin{bmatrix} T_{11} & T_{12} \\ T_{21} & T_{22} \end{bmatrix} \tag{2.12}$$

Thus

$$0 = T_{22} B_{z_0} \tag{2.13}$$

For the potential structure corresponding to the same layer structure, the transfer matrix elements are calculated for different total energy E. To find the energy states in the structure, T_{22} for the different energies is calculated. The eigen energy is correlated to the valley points of T_{22}.

As an example, the absolute value of T_{22} as a function of energy E is plotted in the figure below (Figure 2.2).
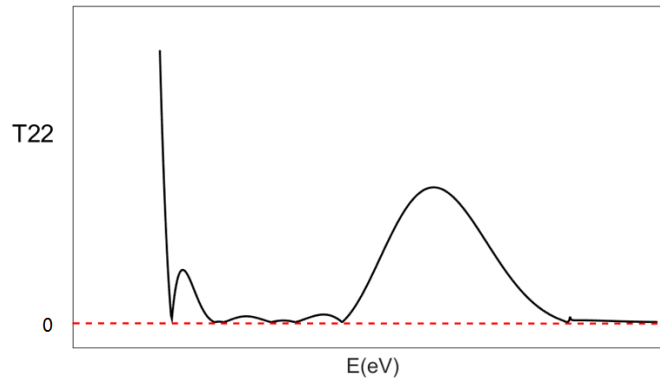
Figure 2.2: The value of the matrix element T_{22}. The zero value points are related to the eigen energies.

Each zero or valley point in the figure correlates to an energy state. To lighten the algorithm, a larger step of energy (1 meV) is used in the first round of calculation to roughly find the locations of states. After that, a refined calculation with a smaller step (0.001 meV) is used to find the exact energy states.

Based on the eigen energies, the matrix F can be easily calculated, [16]

$$F_{(z+\delta z)z} = \frac{1}{2} \begin{bmatrix} (1 + P_{(z+\delta z)z})\exp(ik_{z+\delta z}\delta z) & (1 - P_{(z+\delta z)z})\exp(ik_{z+\delta z}\delta z) \\ (1 - P_{(z+\delta z)z})\exp(-ik_{z+\delta z}\delta z) & (1 + P_{(z+\delta z)z})\exp(-ik_{z+\delta z}\delta z) \end{bmatrix}$$ (2.14)

where

$$P_{z(z+\delta z)} = \frac{m_z^* k_{z+\delta z}}{m_{z+\delta z}^* k_z}$$

For the GaAs/Al$_x$Ga$_{1-x}$As, the experienced value for the effective mass is:

$$m_e^* = (0.067 + 0.083x)m_0$$

$$m_0 = 9.109e - 31 \ kg$$

Normally, to improve the accuracy of the energy calculation, the non-parabolicity effect [17] is supposed to be taken into account. The modified value of the effective mass is:

$$m_{e(non-para)}^* = m_e^* \times (1 + \frac{(E - V(z)}{E_g + \frac{E_{split\,off}}{3}})$$ (2.15)

where

E is the total energy

V is the potential energy

E$_g$ is the band gap energy

E$_{Split\,off}$ is the split off energy

Thus, the wave functions are solved with the matrix F from (2.7)

$$\begin{bmatrix} A_z \\ B_z \end{bmatrix} = \prod_{x=z_0}^{z} F * \begin{bmatrix} A_{z_0} \\ B_{z_0} \end{bmatrix}$$ (2.16)

After normalization, the wave functions can be plotted out. As in Figure 2.3,
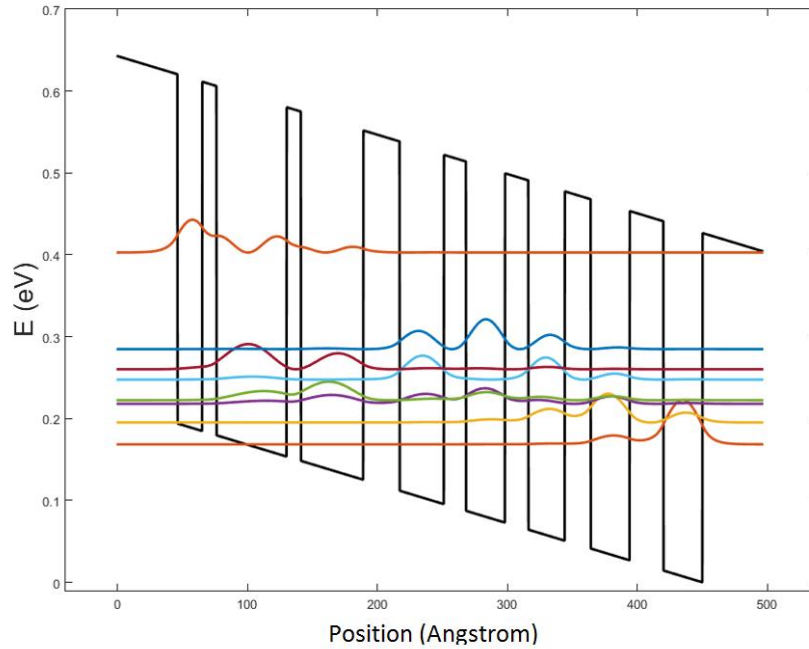
Figure 2.3: Energy states and wave functions of a mid-infrared quantum cascade laser.

2.2 Intersubband Scattering

In the proposed multiple quantum wells structure, electrons are normally trapped in the energy states. The electrons can change status through different scattering processes. Scattering mechanisms, such as phonon scattering, electron-electron scattering and interface roughness scattering, have been widely investigated [18] [19]. By calculating the transition rate of each scattering process, it is possible to know the lifetime of each state, which is a crucial parameter for the theoretical simulation. The two main scattering mechanisms in the mid-infrared quantum cascade lasers are the interface roughness scattering and the longitudinal optical (LO) phonon scattering [20]. Following previous reports, only these two mechanisms are considered in this simulation work.

2.2.1 Interface Roughness Scattering

One popular model for interface roughness scattering was reported by Unuma et al. [21]In this method, the roughness of the interface is described with two parameters, step height Δ and correlation length Λ. The model assumes the relationship as shown [21]

$$\langle \Delta(r)\Delta(r') \rangle = \Delta^2 \exp(-\frac{|r-r'|^2}{\Lambda^2}) \tag{2.17}$$

where r is the coordinate.

Consider two electrons in the subband m, wavevector k' and subband n, wavevector k. The perturbation can be described using the following equation [21]

$$\langle mk'|H_l|nk \rangle = \int d^2 r F_{mn}\Delta(r)\exp(iqr) \tag{2.18}$$

$$q = k - k'$$

$$F_{mn} = V\varphi_m(z)\varphi_n(z)$$

where V is the potential difference and z is the position of the interface. [21]

$$\Gamma_{intra}^{IFR}(E) = \frac{m^* \Delta^2 \Lambda^2}{\hbar^2} \int_0^\pi d\theta \left[\frac{F_{00}}{S(q,T)} - F_{11}\right]^2 \exp(-\frac{q^2\Lambda^2}{4}) \tag{2.19}$$

$$\Gamma_{inter}^{IFR}(E) = \frac{m^* \Delta^2 \Lambda^2}{\hbar^2} F_{01}^2 \int_0^\pi d\theta \exp(-\frac{q'^2\Lambda^2}{4}) \tag{2.20}$$

where

$$q^2 = 2k^2(1 - \cos(\theta))$$

$$q'^2 = 2k^2 + \frac{2m^* E_{10}}{\hbar^2} - 2k\sqrt{k^2 + \frac{2m^* E_{10}}{\hbar^2}}\cos\theta$$

The intersubband and intrasubband scattering rate can also be calculated using the above equations. The values of the parameters of Δ and Λ are missing here. According to a previous study [21], the reasonable values are 3 and 50 Angstrom. These values are highly related to the quality of the growth. In the present

simulation, some alterable values are also used in the range of 3±0.15 and 50±20. Based on the simulated results, Figure 2.4 shows how these parameters affect the scattering time of the interface roughness.
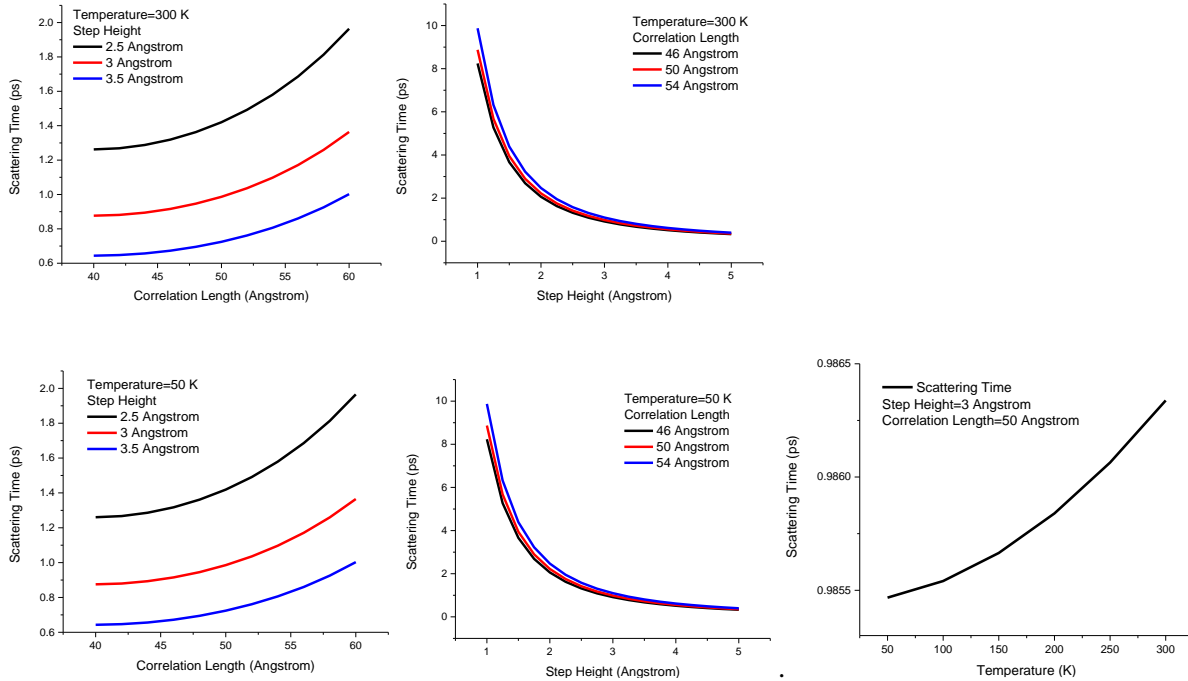
Figure 2.4: Graphical relationship between the interface roughness scattering time, correlation length, step height and temperature.

In Figure 2.4, the effects of the three parameters influencing the interface roughness scattering are shown. As can be seen, the scattering time slightly increases with temperature. However, the scattering time is highly dependent on the correlation length and step height. As can be seen in the graph, smoother interface with lower step height and longer correlation length causes longer scattering time. The profile of the interface is related to the growth quality. Because of the lack of characterization method of material interface, the correlation length and step height in this simulation work is chosen to be the experienced values (~50 and 3 Angstrom).

2.2.2 Longitudinal Optical Phonon Scattering

The scattering caused by longitudinal optical (LO) phonons is another dominant mechanism of transition. The energy of an optical phonon in a material is constant. For example, the optical phonon energy in GaAs is 0.035 eV (corresponding to a wavelength of 35 μm). The transition only happens under a certain condition. For the states $|1k_1\rangle$ and $|2k_2\rangle$ [1] [22]

$$E_2 + \frac{\hbar^2 k_2^2}{2m^*} = E_1 + \frac{\hbar^2 k_1^2}{2m^*} \pm \hbar\omega_{LO} \tag{2.21}$$

Here, the exchanged momentum is set as

$$Q = \sqrt{k_1^2 + k_2^2 - 2k_1 k_2 cos\theta} \tag{2.22}$$

The scattering rate can be written as [1] [22]

$$W_{LO} = \frac{m^* e^2 \omega_{LO} P}{2\hbar^2} \Sigma_f \int_0^{2\pi} d\theta \frac{I^{ij}(Q)}{Q} \tag{2.23}$$

$$P = \frac{1}{\varepsilon_\infty} - \frac{1}{\varepsilon_s}$$

$$I^{ij}(Q) = \int dz \int dz' \psi_1(z)\psi_2(z)e^{-Q|z-z'|}\psi_1(z')\psi_2(z')$$

For GaAs based material system,

$$\varepsilon_\infty = 10.89 \quad \varepsilon_s = 12.9$$

However, the thermal distribution of the phonons is supposed to be considered. The phonons satisfy the Bose-Einstein distribution

$$n_{LO} = \frac{1}{\exp\left(\frac{\hbar\omega_{LO}}{kT}\right)-1} \tag{2.24}$$

Both the absorption and emission of the phonons should be written in the formula. Thus, the total LO phonon scattering rate is [1]

$$W_{tot} = (1 + n_{LO})W_{LO}^{(em)} + n_{LO}W_{LO}^{(abs)} \tag{2.25}$$

Figure 2.5 shows the LO phonon scattering time as a function of temperature and energy difference.
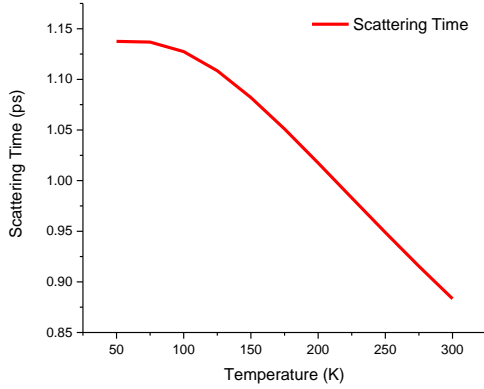
(1)   (2)
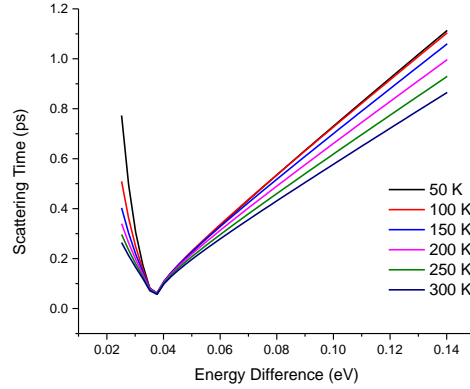
Figure 2.5: (1) The relationship between LO phonon scattering time and temperature. (2) LO phonon scattering time between two states with different separation.

Compared with the interface roughness scattering discussed in 2.2.1, the scattering time of LO phonon scattering is also in picosecond. These two scattering mechanisms are believed to dominate the transition rates in mid-infrared quantum cascade lasers. [1] Similar to the interface roughness scattering, the LO phonon scattering time also slightly depends on temperature. The energy spacing of the states is the most important parameter in the LO phonon scattering. In GaAs material system, LO phonons with energy of 0.035 eV enhances the transition with similar energy difference, which is clearly shown in Figure 2.5 (2). With 0.035 eV energy spacing, the scattering time is much shorter. This effect provides a way to enhance the carrier injection or extraction of certain energy states.

2.3 Transport Modelling

This part presents the method of the transport modelling. The main method used is the rate equation. Although the Monte Carlo method or non-equilibrium Green function (NEGF) might be better in some aspects, the rate equation is still the preferred method for calculating the electron transition in most situations because of the light complexity. The rate equation method could correctly predict the performance of the mid-infrared quantum cascade lasers.

2.3.1 Rate Equation Modelling

Based on the previous study [1], the electron temperature used is 50 K higher than the lattice [23]. This assumption could provide a good prediction of the device performance. The original rate equation for the energy states is: [1]

$$\frac{d\rho_i(t)}{dt} = -\frac{\rho_i(t)}{\tau_i} + \sum_j \frac{\rho_j(t)}{\tau_{j \to i}} \tag{2.26}$$

where

ρ_i is the electron density of the subband i

τ is the transition life time

$$\frac{1}{\tau_i} = \sum_{i \neq j} \frac{1}{\tau_{i \to j}} \tag{2.27}$$

The transition rate between State i and j is determined by the different types of scattering. For the mid-infrared quantum cascade lasers, the two dominant types of scattering are LO-phonon scattering and the interface roughness scattering. The scattering mechanisms are discussed in the subsequent chapters discuss.

The population distribution of the electrons can be written in matrix form as

$$\rho = \begin{bmatrix} \rho_1 \\ \dots \\ \rho_N \end{bmatrix} \tag{2.28}$$

The transition rate involving the N states can be written as [1]

$$V = \begin{bmatrix} -v_1 & v_{2\to1} & \cdots & v_{N-1\to1} & v_{N\to1} \\ v_{1\to2} & -v_2 & \cdots & v_{N-1\to2} & v_{N\to2} \\ \cdots & \cdots & \ddots & \cdots & \cdots \\ v_{1\to N-1} & \cdots & \cdots & -v_{N-1} & v_{N\to N-1} \\ v_{1\to N} & \cdots & \cdots & v_{N-1\to N} & -v_N \end{bmatrix} \tag{2.29}$$

Here, $v = \frac{1}{\tau}$ is used.

A matrix M can be assumed, which makes

$$\Lambda = MVM^{-1}$$

$$\Lambda = diag(\lambda_1, \dots, \lambda_N) \tag{2.30}$$

letting

$$P \equiv M \cdot \rho \tag{2.31}$$

Then, the equation

$$\frac{d\rho}{dt} = V \cdot \rho \tag{2.32}$$

can be changed to

$$\frac{dP}{dt} = \Lambda \cdot P \tag{2.33}$$

Thus, this equation (2.33) can be simplified to

$$P(t) = \exp(\Lambda t) \cdot P(0) \tag{2.34}$$

Therefore

$$N(t) = M^{-1} \cdot \exp(\Lambda t) \cdot M \cdot N(0) \tag{2.35}$$

As the definition of the transition rate,

$$\sum_{j \neq i} v_{i \to j} = v_i \tag{2.36}$$

23

The eigen values of the matrix V are not supposed to be larger than 0. Thus, in the long time limit, all the elements of exp(Λt) will converge to zero except the one corresponding to the 0 eigen value.

$$\exp(\lambda_1 = 0) = 1 \tag{2.37}$$

$$\exp(\Lambda t) = diag(1,0,\dots,0) \tag{2.38}$$

The stationary solution of the population distribution is

$$\lim_{t \to \infty} N(t) = M^{-1} diag(1,0,\dots,0) M \cdot N(0) \tag{2.39}$$

Which is proportional to the eigen vector β_1 related to the 0 eigen value, which means

$$V \cdot \beta_1 = 0 \tag{2.40}$$

$$N(\infty) \propto \beta_1 \tag{2.41}$$

Based on the scattering time calculated in 2.2, the transition rates among the states are obtained with (2.27). Thus equations (2.28)-(2.41) show a method to solve the rate equation (2.26). With the help of this implementation, the carrier distribution among the states can be solved. By multiplying the doping density with the normalized result of (2.41), the carrier density in each state is calculated.

2.3.2 Current Density Calculation

If the first order tunneling is assumed, the tunneling time can be expressed as (2.42) [3]

$$T = \frac{1+\Delta^2 \tau_\parallel^2}{2\Omega^2 \tau_\parallel} \tag{2.42}$$

Where

$\hbar\Delta$ and $\hbar\Omega$ are the detuning energy and coupling energy

$$\hbar\Delta_{12} = (E_1 + \int \psi_1 V_2 \, \psi_1 dx) - (E_2 + \int \psi_2 V_1 \, \psi_2 dx) \tag{2.43}$$

$$\hbar\Omega_{12} = \frac{1}{2}\sqrt{(E_1 - E_2)^2 - (\hbar\Delta)^2} \tag{2.44}$$

$\tau_\parallel$ is called the dephasing time, defined as

$$\tau_{\parallel 12} = \frac{2\hbar}{\Gamma_{tun}^{12}} \tag{2.45}$$

$$\Gamma_{tun}^{12} = \frac{1}{2}\left(\Gamma_{intra}^{12} + \Gamma_{inter}^{1} + \Gamma_{inter}^{2}\right) \tag{2.46}$$

Γ can be calculated though the different scattering mechanisms. This is also called energy broadening. This value is also used to calculate the gain spectrum.

So far, here is the equation for the current density in a two level system:

$$J = eN_{2D}\frac{\rho_1 - \rho_2}{T} = eN_{2D}\frac{2\Omega_{12}^2\tau_{\parallel 12}}{1 + \Delta_{12}^2\tau_{\parallel 12}^2 + 4\Omega_{12}^2\tau_2\tau_{\parallel 12}} \tag{2.47}$$

In a more practical case with multiple states (N) in each module:

$$J = \sum_{j=1}^{N}\sum_{i=1}^{N}eN_{2D}\frac{\rho_i - \rho_j}{T} = \sum_{j=1}^{N}\sum_{i=1}^{N}eN_{2D}\frac{2\Omega^2\tau_\parallel(\rho_i - \rho_j)}{1 + \Delta^2\tau_\parallel^2} \tag{2.48}$$

To verify the simulation method, Figure 2.6 shows the simulated current-voltage curve based on equation (2.48) from the self-developed program compared to the experimental data from the reference [13]. In the calculation, the value of Schottky potential is assumed to be around 0.7 volts [24].
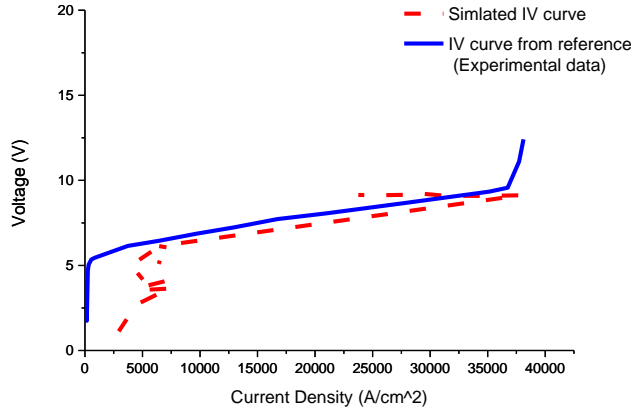
Figure 2.6: Comparison of the simulated current-voltage curves with the experimental result [13].

As Figure 2.6 shows, the simulated IV curve (red dash line) is comparable with the experimental data (blue line). This simulation does not work well in the region with low and high bias. Since the simulation is focused on the electrical performance of the quantum structure, the doping profile in the bulk material is not considered. Additionally, with high bias, the negative differential resistance effect may damage the electrical performance, which is not included in the simulation program. Collectively, the simulation result is believed to be a method that predicts and analyse the lasers' performance.

2.3.3 Oscillator Strength Calculation

The oscillator strength is a quantity describing how the wave functions are overlapped. Based on Fermi's Golden Rule, its value is related to the intensity of the transition. Mathematically, the optical gain between two states is proportional to the oscillator strength. In this work, the oscillator has the following expression (2.49):

$$f_{12} = \frac{2|\langle \psi_1 | P | \psi_2 \rangle|^2}{m^*(E_a - E_b)} \tag{2.49}$$

where P is the momentum operator.

2.3.4 Optical Gain Calculation

In the optical gain materials with population inversion, the gain value is greatly dependent on the transition rate. Fermi's Golden Rule is a useful tool to calculate the probability of the transition:

$$\Gamma_{1\to2} = \frac{2\pi}{\hbar}|\langle2|H'|1\rangle|^2\rho_2 \tag{2.50}$$

where H$^{'}$ is the perturbation matrix

In the case of mid-infrared quantum cascade lasers, the optical gain can be described as (2.51)

$$g = \frac{\pi\hbar e^2}{2n_r c\mathcal{E}_0 m^*}f(N_2 - N_1)\mathcal{L}(\hbar\omega - \Delta_{21}) \tag{2.51}$$

where $(N_2 - N_1)$ is the population inversion, the Lorentzian function $\mathcal{L}$ is introduced to describe the broadening of the optical transition. Figure 2.7 shows the calculated results of the peak gain at various temperatures and the gain spectrum based on (2.51). The sample structure is from reference [13].

(1) (2)
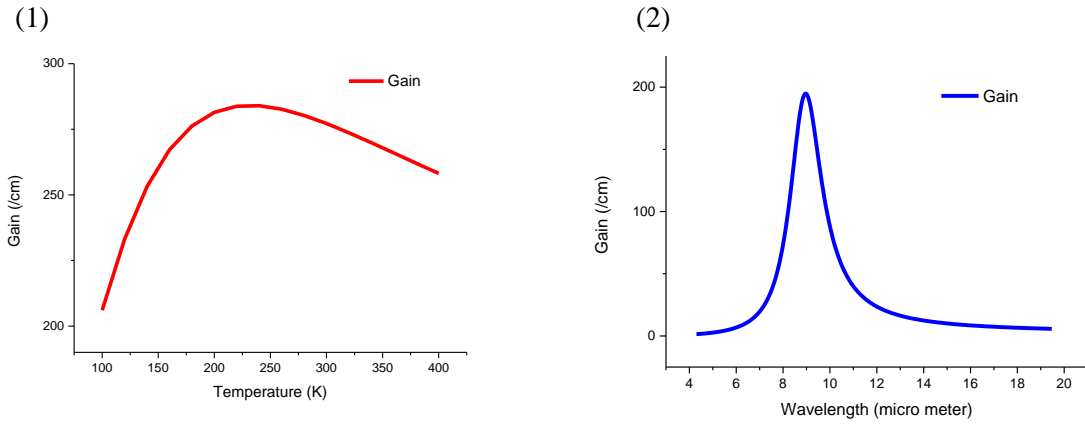
Figure 2.7: (1).The relationship between optical gain and temperature using an electrical field of 4.8 kV/cm. (2). Gain spectrum with 100 K temperature and 4.8 kV/cm electrical field.

The optical gain simulation is supposedly a tool for predicting the temperature performance and spectrum. In Figure 2.7, the simulation results are based on the structure from the reference [13]. It is also one structure reported in this work. According to Figure 2.7 (1), this mid-infrared laser shows high optical gain even at a high temperature (above room temperature). Thus, it is expected to be a room temperature operating mid-infrared quantum cascade laser, which is verified in reference [13]. In Figure 2.7 (2), the peak center is around 9 μm, which is the same with the experimental results. The simulation program

developed here shows the ability to analyse and predict the performance of mid-infrared quantum cascade lasers. Both the electrical and optical performance can be solved through the program.

2.4 Hartree Potential

Considering the carrier density in mid-infrared quantum cascade lasers, a 10^{16}cm^{-3} doping will provide a similar amount of electrons in the conduction band. The potential caused by the distribution of carriers should be taken into account to improve the accuracy of the energy states calculation. The Hartree potential describes the electron-electron interaction, also known as the screening effect. This potential affects the energy structure especially when the electrons and donors are separated spatially.

The Hartree potential can be treated as the electrical potential caused by the charge distribution in a period structure. The pure charge distribution is described as:

$$\rho(z) = eN_D(z) - e \sum_i n_i |\varphi_i(z)|^2 \qquad (2.52)$$

where N_D is the doping density as a function of location.

n_i is the carrier density in the state i.

The Hartree potential V_H can be calculated using the following equation:

$$\frac{\partial^2 V_H(z)}{\partial z^2} = -4\pi n(z) \qquad (2.53)$$

The carrier distribution is solved by the transport modelling method discussed in 2.3. However, the contribution of the Hartree potential changes the condition of the Schrödinger equation. Thus, the final solution of this problem is to perform the calculation in a self-consistent loop. The Hartree potential should be added on top of the static potential, as shown in Figure 2.8. After solving the Schrödinger equation and the transport status, a new Hartree potential can also be calculated with the charge distribution. As in Figure 2.8, the Hartree potential causes a slight shift of the energy structure. This effects a lot when doping density is relatively high. However, considering the algorithm, this self-consistent loop consumes calculation time and space. Therefore, It is reasonable to limit the loop running time.

(1)

(2)
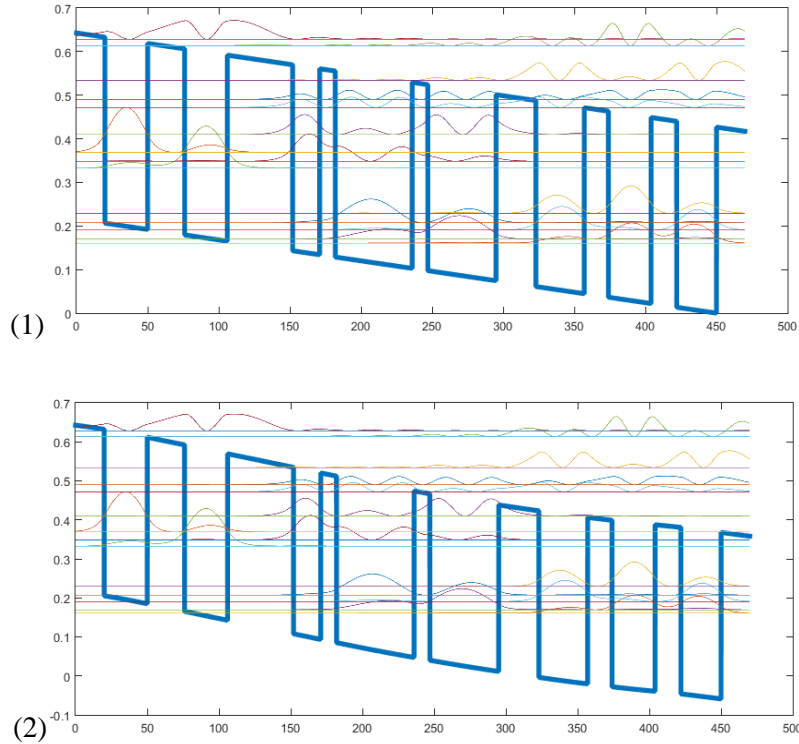
Figure 2.8: The energy structure without (1) and with (2) Hartree potential. The additional potential curves the static potential.

2.5 Summary

The whole simulation processes are discussed in this chapter. From the energy structure of the layered materials, the Schrödinger equation is solved with the transfer matrix method. Scattering time is calculated based on the energy states and wave functions from the Schrödinger equation. As an integrated effect of the different scattering mechanisms, the transition rates and carrier distribution among the states are implied with the rate equation method. Thereafter, the electrical and optical profiles of the mid-infrared quantum cascade lasers can be calculated. The simulation method is verified by comparing the theoretical results with the published references in the previous parts of the chapter. The simulation results are believed to be reliable.

As a complicated quantum system, the theoretical study of mid-infrared quantum cascade lasers is still under investigated [19] [21]. In this chapter, the simulation method introduced is a basic and simplified strategy. The simulation works can be improved from several aspects. Firstly, more scattering

mechanisms can be introduced to the calculation. Although the interface roughness scattering and the LO phonon scattering are trusted to be the dominants, other effects, such as LA phonon and electron-electron scattering, also influence the transition rate. More accurate simulation may contain more scattering mechanisms. Secondly, the rate equation is the widely used method for finding the carrier distribution, but not the only way. The Non Equilibrium Green's Function and Monte Carlo Method are also reported to be reliable methods. Thirdly, the effects of photons are supposed to be considered for lasing simulation. Photons were ignored in the previous simulation. More and more complete simulation method may demonstrate more knowledge about the quantum systems.

Chapter 3

Experiment Setup

3.1 LIV Measurement Setup for MIR QCL

To measure the electrical and optical features of the lasers in this study. The light-current-voltage (LIV) measurement system was designed as shown in the Figure 3.1.
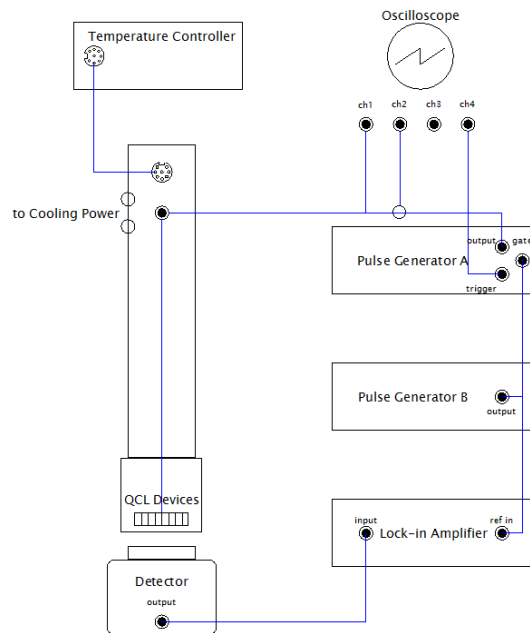
Figure 3.1: Block diagram of our Light-Current-Voltage (LIV) measurement system

For most of the mid-infrared quantum cascade lasers, the temperature of the best performance is normally lower than room temperature (~295 K). Hence, a cryostat with a temperature controller is used to set the working temperature to the desired value. A closed cycle liquid Helium cooling pump is applied as the cooling power of the vacuum system. The MIR QCL devices are fixed on a seven-pin gold coated package to achieve strong electrical and thermal contact. The whole vacuum system can be cooled down to ~10K. With the proportional-integral-derivative (PID) temperature controller, the temperature can be stable at any point between 10K and 350K.

The LIV measurement is done in pulse mode with pulse generator A (AVTECH) as the power supply for the MIR QCL devices. Normally 500-2000Hz, 250-1000ns are used as the parameters of the voltage pulse. The voltage and current through the electrodes of the MIR QCLs are measured using an oscilloscope (Tektronix MDO3054). Channel 1 and 2 on the oscilloscope correspond to the voltage and current signal. Channel 4 acts as the trigger signal of the oscilloscope to synchronize the signal. The response time of some detectors is too long, so that they may not be able to catch the signal of 500-2000Hz. For this reason, pulse generator B is used as the gate of pulse generator A. The typical parameters we used for pulse generator B are 20 Hz as the frequency and 25 ns as the pulse width (shown in the Figure 3.2).
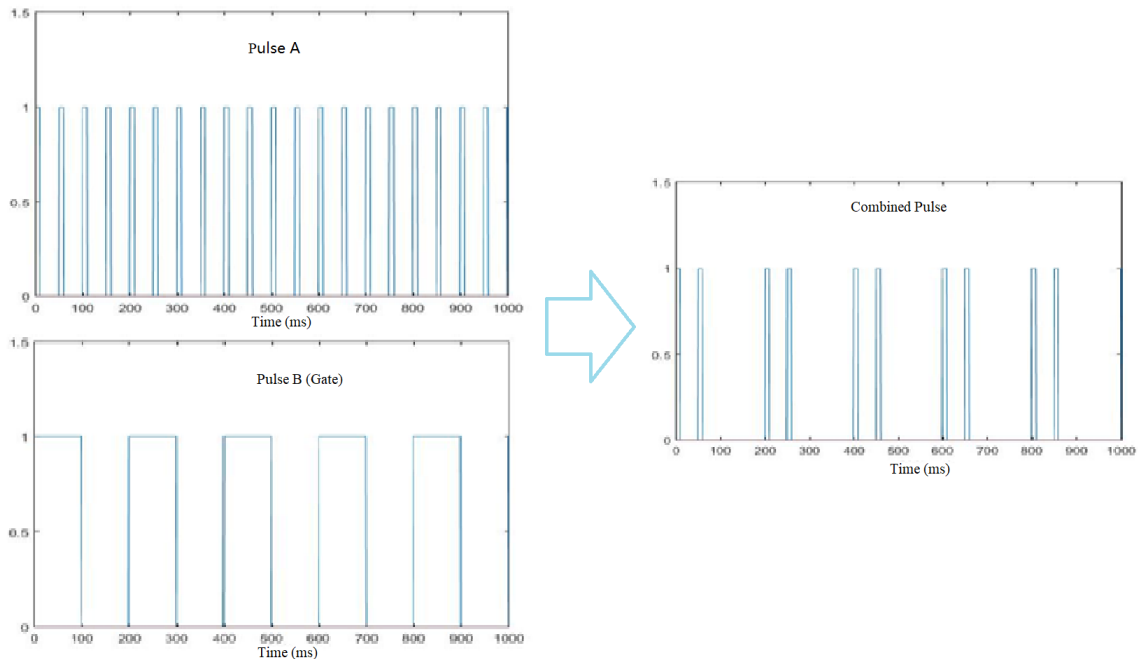
Figure 3.2: Example of the pulse shape of the pumping voltage on the device.

To measure the mid-infrared light source, an InSb/MCT detector (Teledyne Judson j15d14insbm204s01m) is used. The responsivity of the detector is shown below in Figure 3.3. Both of the detectors inside are supposed to work at the temperature of liquid nitrogen (77 K).

Relative Response vs Wavelength
for J15InSb Series "Sandwich" Detector
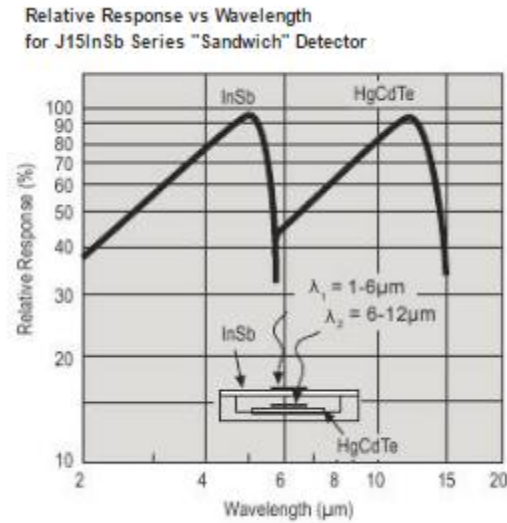
Figure 3.3: Relative responsivity of an InSb/MCT detector with different wavelength. [25]

For light with a wavelength of 1-5.5 µm, the InSb detector has good efficiency. It is a self-supplied device which can generate output current with no external bias voltage.

Because the bandgap of InSb is about 0.17 eV (corresponding to the wavelength of 7.2 µm), the performance of the InSb detector is poor for photons with wavelength longer than 7 µm. Thus, a mercury cadmium telluride (MCT) detector is used for the lower energy photons. Since the MCT detector require external bias to work, a circuit, as in Figure 3.4, is designed to provide the voltage and collect the electrical signal from the detector.
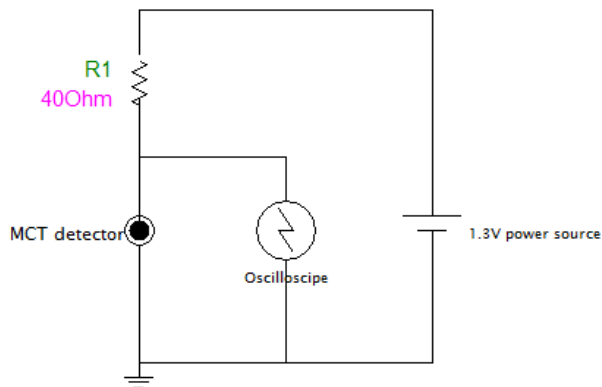
Figure 3.4: The outer circuit connected to the MCT detector to provide bias and collect data.

By using this self-designed circuit, long wavelength of(6-12 µm) mid infrared light can be detected and shown on the oscilloscope (channel 3), the waveform is shown in Figure 3.5.
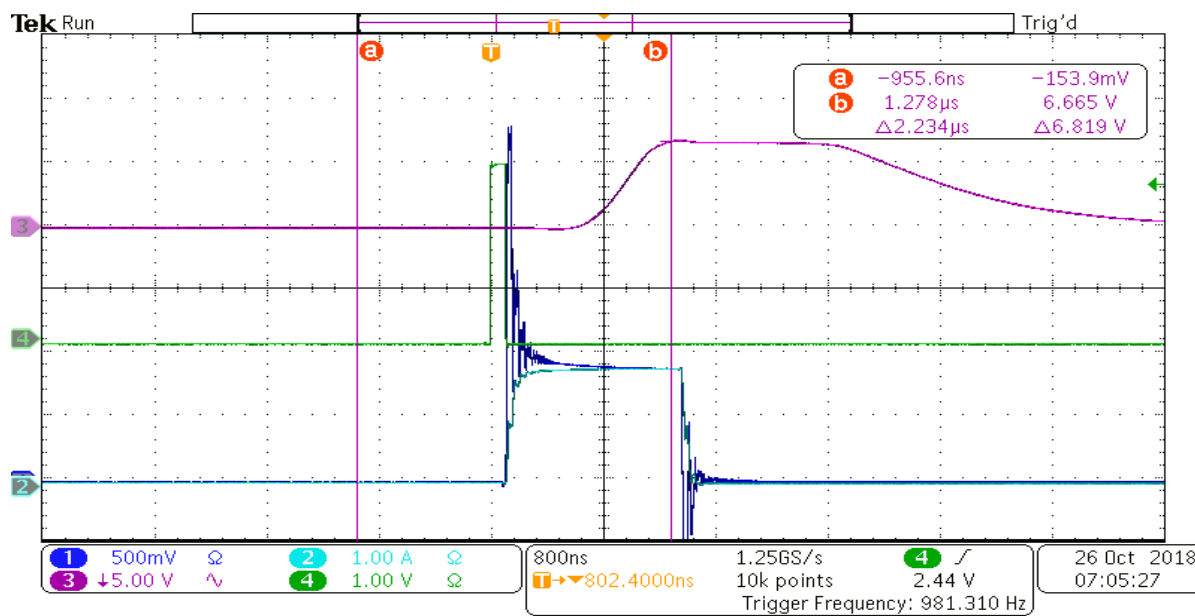
Figure 3.5: The waveform collected from the oscilloscope. Channel 1 is proportional to the voltage applied on the device. Channel 2 is the current through the devices, and Channel 3 is the light signal for the detector.

3.2 Spectrum Measurement
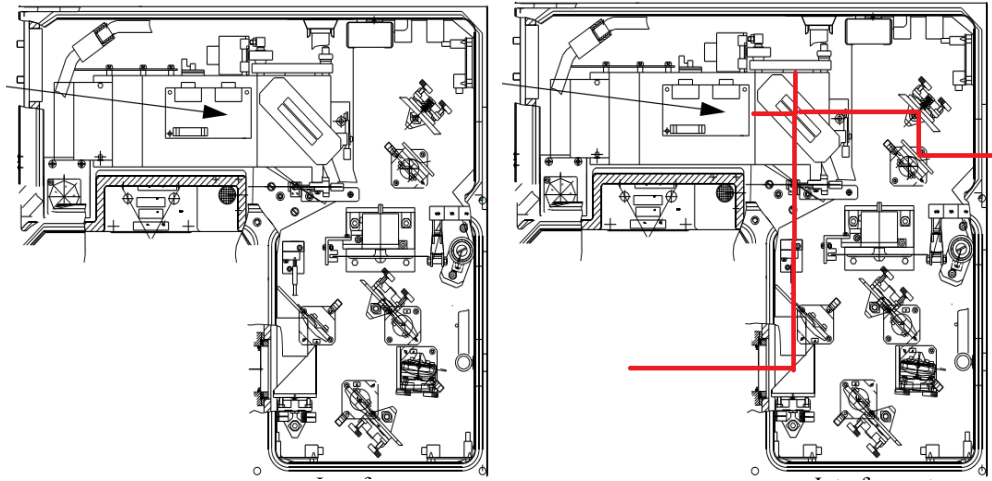
Figure 3.6: The structure of the Fourier-transform infrared spectroscopy (FTIR) system. The optical path is highlighted with red lines.

Fourier-transform infrared spectroscopy (FTIR) is a widely known technique used to obtain the infrared transmission or absorption spectrum. The lasing spectrums of the mid-infrared quantum cascade lasers are tested using FTIR spectrum (from Bruker). The optical path is shown in Figure 3.6.

3.3 Detecting System Calibration

To obtain the actual output power of the proposed mid-infrared quantum cascade lasers, the detecting systems are supposed to be calibrated. A black body radiator is used as the standard power source for the detector calibration. The spectrum of the black body radiation depends only on the temperature.

According to Planck's law of black body radiation,

$$B_\nu(T) = \frac{2h\nu^3}{c^2} \frac{1}{e^{\frac{h\nu}{kT}} - 1} \qquad (3.1)$$

Where

B is the spectral radiance

c is the speed of light

h is the Planck constant

k is the Boltzmann constant

T is the absolute temperature of the black body

ν is the frequency of the radiated photons

The basic relationship

$$c = \lambda\nu \qquad (3.2)$$

Where

λ is the wavelength of the photons

The intensity of the black body radiation at different temperatures is shown below in Figure 3.7.

Thus

$$\mathrm{d}v = -\frac{c}{\lambda^2}d\lambda \tag{3.3}$$

$$B_\lambda(T) = \frac{2hc^2}{\lambda^5}\frac{1}{e^{\frac{hc}{\lambda kT}}-1} \tag{3.4}$$

Here, the B_λ is plotted at 300-1000K in Figure 3.7.
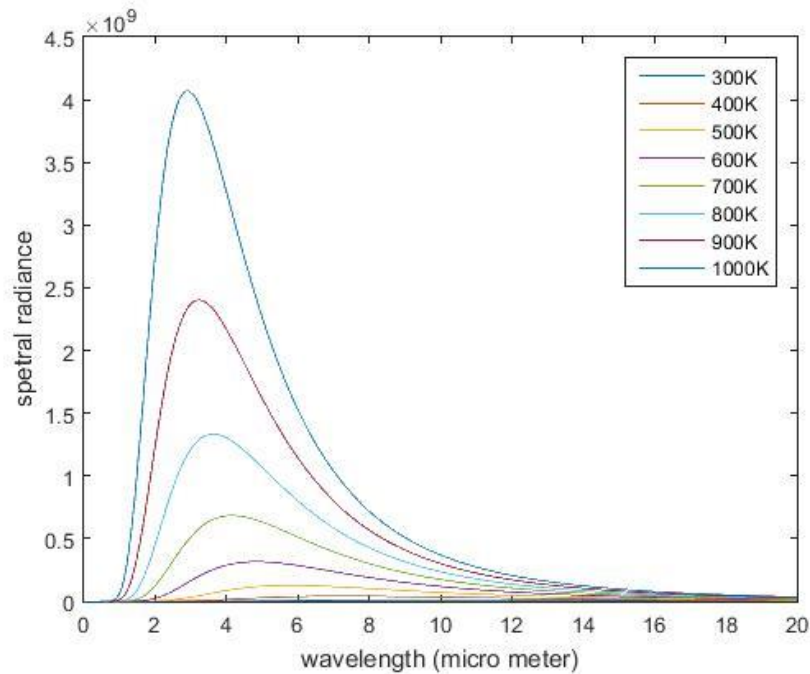
Figure 3.7: Spectrum of black body radiation, calculated at various temperatures.

It can be noticed that the peak power of a black body radiation is rightly located in the mid-infrared range. Here, 500-1000 K black body radiation is selected as the standard light source to calibrate the detecting system.
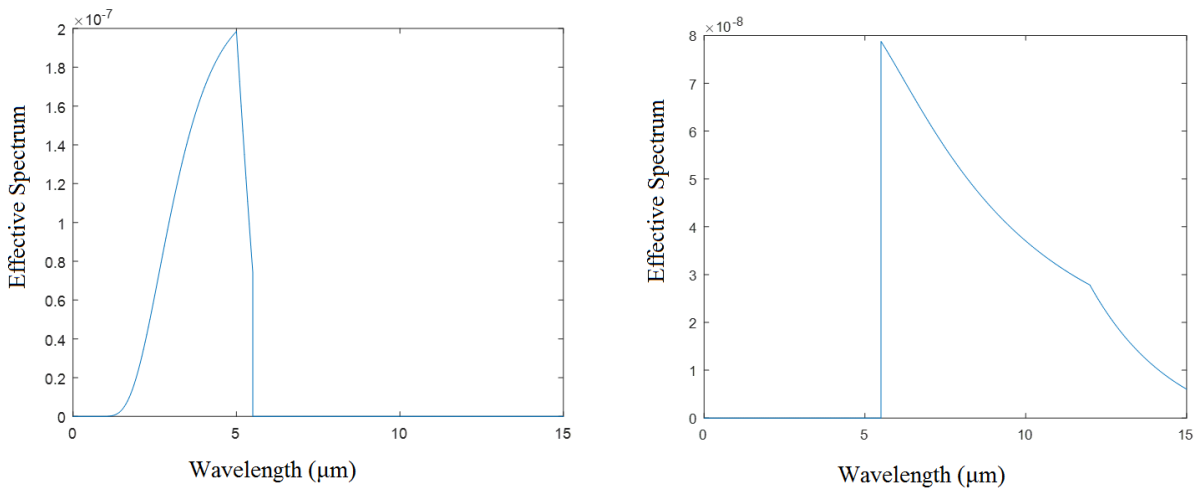
Figure 3.8: The effective power spectrum of black body (integration of responsivity multiplied by black body spectrum).

The shapes of the responsivity of the detectors are assumed to be the same with the design curves. Compared with the responsivity in Figure 3.3 [25], the effective power is supposed to have the shapes in Figure 3.8. To calibrate the detectors, the output electrical signal is measured. Compared to the integral of effective power, as in the fitting curves in Figure 3.9, the responsivity of the whole system can be obtained as listed below in Table 3.1.

Tempearature	Current data	Voltage d	Weff (0-5.5u	Weff2 (5.5-15um
400	0.07	0.5	8.4953E-6	4.648E-5
450	0.18	0.95	2.0795E-5	7.3066E-5
500	0.39	1.5	4.3348E-5	1.0629E-4
550	0.7	1.8	8.0323E-5	1.4586E-4
600	1.2	2.1	1.3616E-4	1.9135E-4
650	1.9	2.2	2.1544E-4	2.4226E-4
700	2.6	2.6	3.2277E-4	2.9807E-4
750	4	3	4.6272E-4	3.583E-4

Table 3.1: Calibration of data at different temperatures of black body. Voltage d is the measured light signal. Weff and Weff2 are the effective power (integration of spectrum and responsivity) in different range (0-5.5 and 5.5-15 μm).
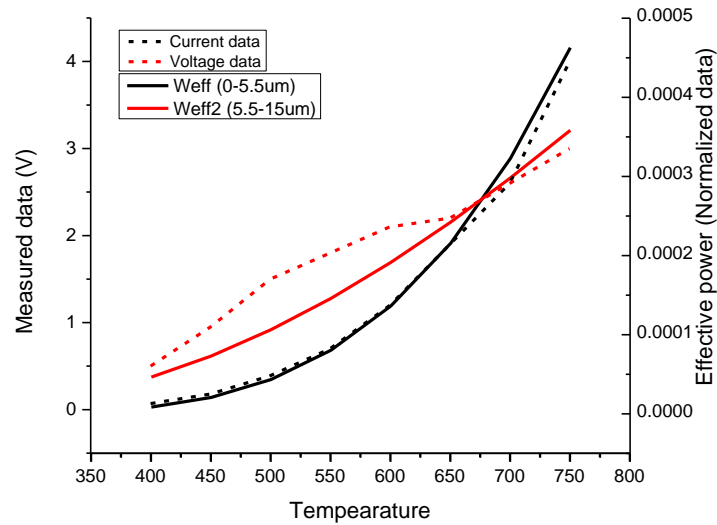
Figure 3.9: Fitting curves of calibration.

To verify the assumption of the shape of the response efficiency. The collected current and voltage signal from the system are compared with the calculated effective power (Weff and Weff2) in Figure 3.9. As the figure shows, the calculated effective power follows the trend of the experimental data. Thus, the basic assumption is certified to be reliable.

3.4 Device Packaging

To mount the mid-infrared quantum cascade lasers on the cold finger of the cryostat and complete the electrical connection, metal holders are designed and made, shown in Figure 3.10.

The copper pieces are fabricated in a specific shape. After cutting and polishing, the copper pieces are coated with gold by electroplating. The parts with seven gold pins are glued on the gold coated surface with silver epoxy. During the performance testing, the MIR QCLs are cleaved into 1 cm * ~2mm pieces with 10-15 lasers on the top surface of each piece. To achieve high quality thermal conduction, the Indium solder is placed underneath the cleaved material. The wire bonding machine (K&S Inc. 4523) is used to connect the electrodes on the devices and the pins.
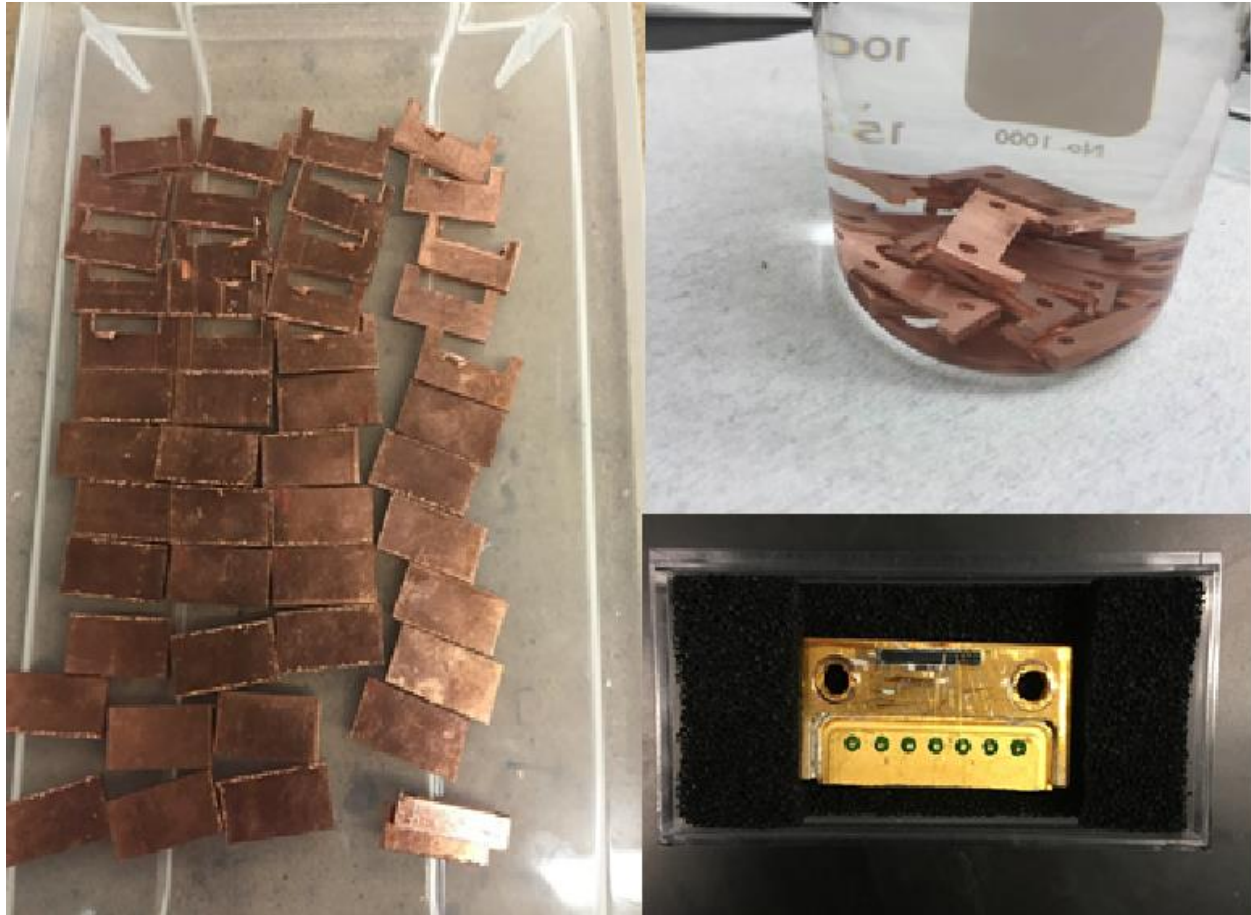
Figure 3.10: The thermal conductive sample holder. (From metal pieces to gold coated parts)

3.5 Cryogenic Station

The structure of the cryostat used in the lab is shown in Figure 3.1. The outer shell is made of aluminum alloy. Heat conduction is achieved with a copper cold finger placed in the center of the vacuum chamber. The device under test is mounted on the copper package and fixed on the cold finger. The temperature of the cryostat is cooled with a He-cycled cooling pump and vacuumed with a two-level mechanic/molecular pump. The best vacuum pressure obtained in this system is 10^{-7} mTorr at ~10K, and the lowest temperature is ~8K which is good enough for most of the MIR QCLs characterization. The temperature is measured using the two thermal couples on the cold finger. To control the temperature, a resistance wire

is connected on the copper cold finger for heat supply. The heating power is controlled with a proportional-integral-derivative (PID) temperature controller. Normally, the feedback loop provides a very stable temperature with variation of 0.001K.

In the front of the vacuum chamber, the light from the MIR QCLs is released through a mid-infrared window. The material of the window is normally KBr. For measurement of 3-5 μm light, a CaF_2 window can also be used. The absorption spectrum of these two material is shown in Figure 3.11.
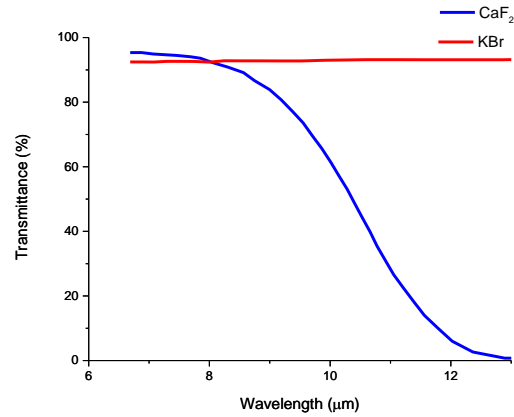
Figure 3.11: Transmission spectrum for different materials of the windows. Compared to CaF_2, KBr window shows a significant advantage in longer (6-15 μm) mid-infrared wavelength [26].

3.6 Beam Pattern Measurement

A setup is used to measure the beam pattern of the light from the lasers as shown in Figure 3.12. In this setup, the photon detector is connected with a 2-D motion controller. Thus, the light intensity is measured at different positions. The beam pattern indicates much information about the light field. In some applications, such as long path gas sensing, the collimation of the laser is critical. This measurement helps to know the performance of the devices.
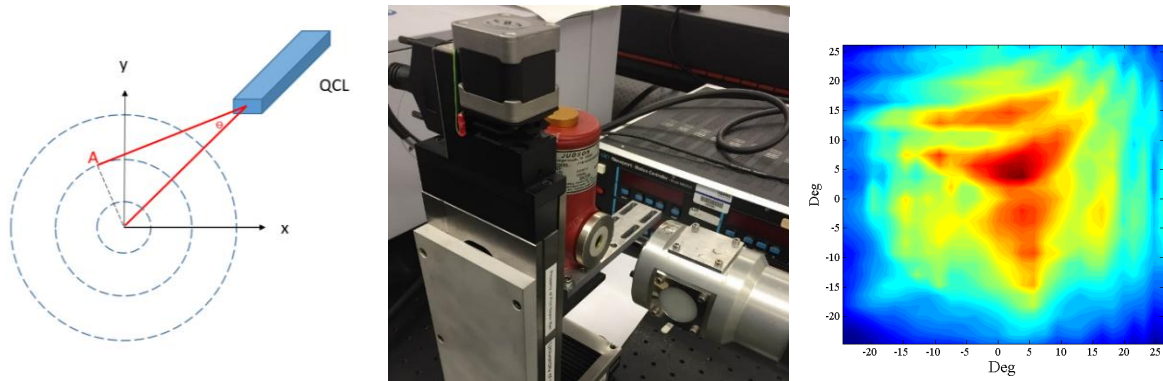
Figure 3.12: Experimental setup and result of beam pattern measurement

As shown in Figure 3.12, to measure the output power at various position, the optical detector is mounted on a holder with a motion controller. During the measurement, the detector moves in a plane. And at point, say point A for example, the light intensity is collected and recorded. With the different angle Ө, the light intensity from the lasers is expected to be vary. The information of the light divergence can be obtained from the measurement results.

3.7 Temperature Dependent Measurement

To improve the accuracy of the measurements, the tests are repeated as many times as possible, for example, 1000 scans are performed for spectrum measurements and 100 scans for IV measurements. The Labview programs help us to control the systems. For many MIR QCLs, the performance is measured at different temperature. Here, a temperature controlling program is developed to automatically set the temperatures. It can be added to most of the controlling programs to achieve the measurements at different temperature. The block diagram is shown in Figure 3.13.
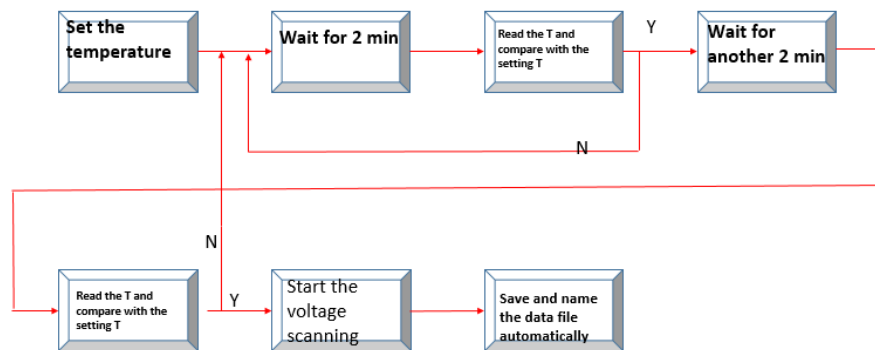
Figure 3.13: Block diagram of the temperature controlling program

Chapter 4

Experimental Results

4.1 Devices Overview

Based on the different lattice constants, the mid-infrared quantum structures of the lasers are grown on InP or GaAs substrates.

Left growth sheet (Semi Insulating GaAs):

Comment	Material	x	d [A]	doping N [cm-3]	reps
Emitter	GaAs		10000.00	5.00E+18	1
cladding	GaAs		35000.00	5.00E+16	1
Injector region	AlxGa1-xAs	0.45	28.00		1
Injector region			34.00		1
Injector region	AlxGa1-xAs	0.45	17.00		1
Injector region			30.00	4.00E+17	1
Injector region	AlxGa1-xAs	0.45	18.00		1
Injector region			28.00		1
Injector region	AlxGa1-xAs	0.45	20.00		1
Injector region			30.00	4.00E+17	1
Injector region	AlxGa1-xAs	0.45	26.00		1
Injector region			30.00		1
Injector Barrier	AlxGa1-xAs	0.45	44.00		35
Active region	GaAs		20.00		35
Active region	AlxGa1-xAs	0.45	12.00		35
Active region	GaAs		54.00		35
Active region	AlxGa1-xAs	0.45	10.00		35
Active region	GaAs		48.00		35
Extraction Barrier	AlxGa1-xAs	0.45	28.00		35
Injector region	GaAs		34.00		35
Injector region	AlxGa1-xAs	0.45	17.00		35
Injector region	GaAs		30.00	4.00E+17	35
Injector region	AlxGa1-xAs	0.45	18.00		35
Injector region	GaAs		28.00		35
Injector region	AlxGa1-xAs	0.45	20.00		35
Injector region	GaAs		30.00	4.00E+17	35
Injector region	AlxGa1-xAs	0.45	26.00		35
Injector region	GaAs		30.00		35
Injector Barrier	AlxGa1-xAs	0.45	44.00		1
Cladding	GaAs:Si		35000.00	5.00E+16	1
Collector	GaAs:Si		10000.00	5.00E+18	1

Right growth sheet (N+ InAs):

| Comment	Material	d [A]	doping	reps
Your Buffer, if needed	InAs:Si	x	1.0E+18	
Plasmonic cladding (ground contact)	InAs:Si	18000.00	5.0E+19	
Superlattice spacer	AlSb	20.00		200
	InAs:Si	20.00	1.0E+17	200
1st injector	AlSb	15.00		
	InAs	25.00		
	AlSb	10.00		
	InAs:Te	23.00	4.0E+17	
	AlSb	10.00		
	InAs:Te	21.00	4.0E+17	
	AlSb	11.00		
	InAs:Te	21.00	4.0E+17	
	AlSb	13.00		
	InAs:Te	21.00	4.0E+17	
	AlSb	15.00		
	InAs:Te	20.00	4.0E+17	
	AlSb	17.00		
	InAs:Te	20.00	4.0E+17	
	AlSb	18.00		
	InAs	19.00		
	AlSb	19.00		
	InAs	18.50		
Injector Barrier, b0	AlSb	27.00		24
w1, active wells	InAs	41.00		24
b1, active wells	AlSb	9.00		24
w2, active wells	InAs	36.00		24
b2, active wells	AlSb	9.00		24
w3 active well	InAs	34.00		24
b3, active wells	AlSb	12.00		24
w4, active wells	InAs	28.00		24
b4, active wells	AlSb	10.00		24
w5, active wells	InAs	25.00		24
b5, active wells	AlSb	10.00		24
INJECTOR REGION	InAs:Te	23.00	4.0E+17	24
	AlSb	10.00		24
	InAs:Te	21.00	4.0E+17	24
	AlSb	11.00		24
	InAs:Te	21.00	4.0E+17	24
	AlSb	13.00		24
	InAs:Te	21.00	4.0E+17	24
	AlSb	15.00		24
	InAs:Te	20.00	4.0E+17	24
	AlSb	17.00		24
	InAs:Te	20.00	4.0E+17	24
	AlSb	18.00		24
	InAs	19.00		24
	AlSb	19.00		24
	InAs	18.50		24
Superlattice spacer	AlSb	20.00		200
	InAs:Si	20.00	1.0E+17	200
Plasmonic cladding (Positive Top contact)	InAs:Si	15000.00	5.0E+19	

Figure 4.1: Growth sheets of the GaAs and InP based lasers. The thicknesses, materials and doping densities of each layers are shown.

Figure 4.1 is an example of the grown layered structure. The core quantum structure is sandwiched between two cladding layers. The material is partly doped with Si to achieve Ohmic contact with the

electrodes. In the active region, some of the quantum wells are also doped to provide carriers, so that the lasing transitions can occur while the carriers travel through the layers.
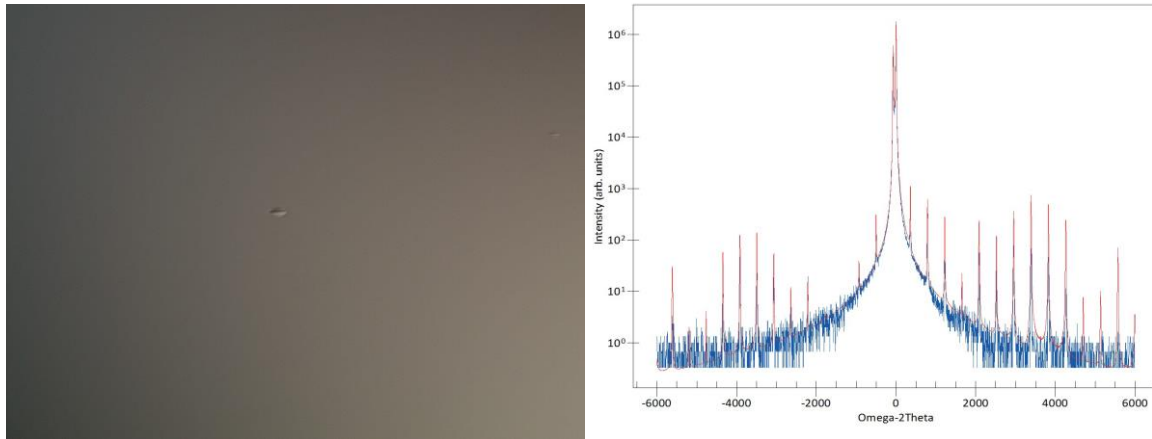
Figure 4.2: Microscopic picture and X-Ray diffraction results. These post-growth characterization give us more information about the quality of the wafers.

After the growing process, X-Ray diffraction (XRD) is used to detect the quality of the material as shown in Figure 4.2. In the microscopic photo, defects with micrometers size can be seen on the surface. The XRD results show how the grown layers thicknesses differ from what was designed.

Before fabrication, the wafers are cleaved into pieces (~1 cm × 1 cm each), as Figure 4.3.
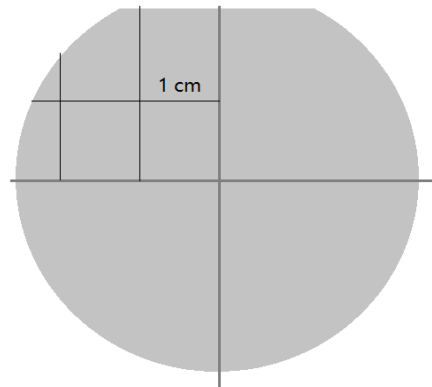
Figure 4.3: Schematic figure of the cleaved wafer. The wafer is cut into ~1 cm × 1 cm pieces before fabrication.
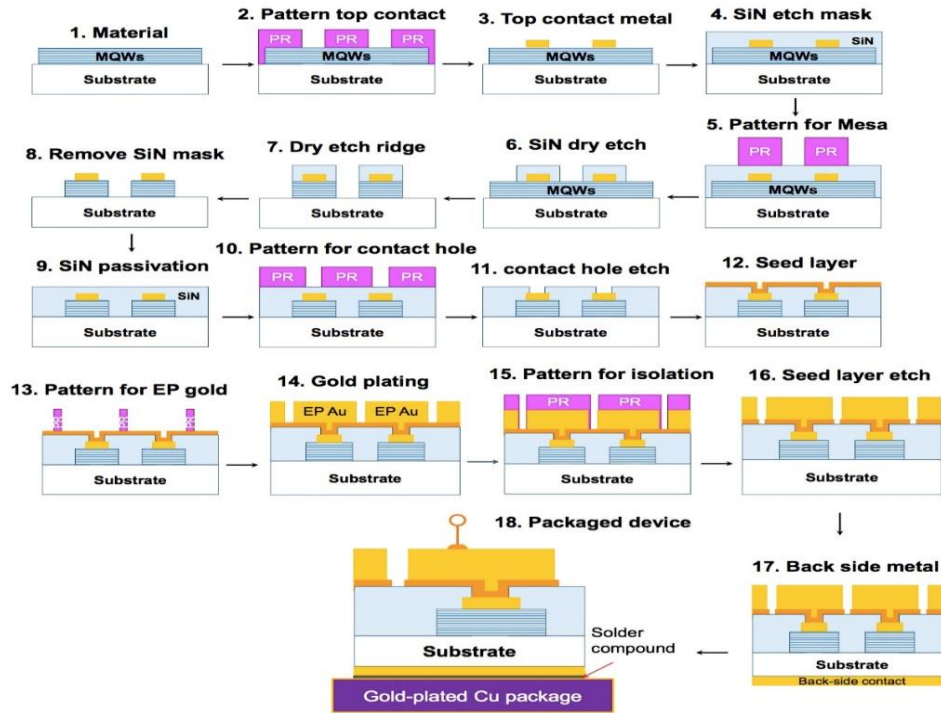
Figure 4.4: Block diagram of the processes for fabricating mid-infrared quantum cascade lasers. [15]

After the fabrication processes as described in Figure 4.4 (Same with Figure 1.10), the mid-infrared quantum cascade lasers are made into two types of shape, round disks and rectangle ridges.

As shown in Figure 4.5, the epitaxy layers are fabricated into individual shapes. Because highly doped substrates are used, the top and bottom surfaces could function as the electrodes. The cuboid and cylinder parts act as the waveguide of the mid infrared light travelling in the material.
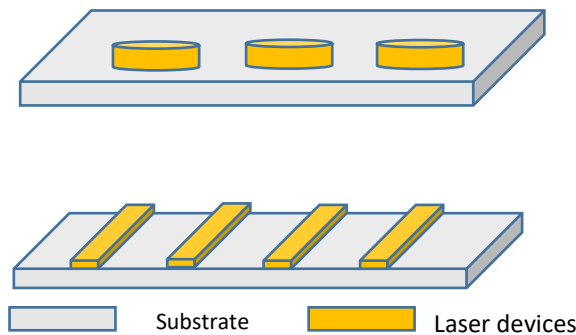
Figure 4.5: 3-D sketch of the fabricated disk and ridge shaped mid-infrared quantum cascade lasers

4.2 Disk Devices

The quality of the wafers used at the beginning of the project were not good enough. Moreover, the success rate of the fabrication processes was low. To overcome these influence of the defects, the disk shapes are used as the waveguide at the beginning. Thus, the performance of the disk devices is used as a referee to improve the fabrication processes. As a result, several wafers are made into disk shape lasers, listed in Table 4.1.

Wafer Number	Piece Number
G0144	①④
G0160	①
G0173	①
G0162	①
G0212	①
G0214	③

Table 4.1: List of the disk mid-infrared quantum cascade lasers.

Since the round shape has no directional selectivity, the light is emitted from the whole sidewall of the disk and the intensity equally distributed in different direction. Thus, the light collected from this type of laser is not strong. As a prototype, the disk lasers are used to verify the feasibility of the growth, fabrication and testing process.
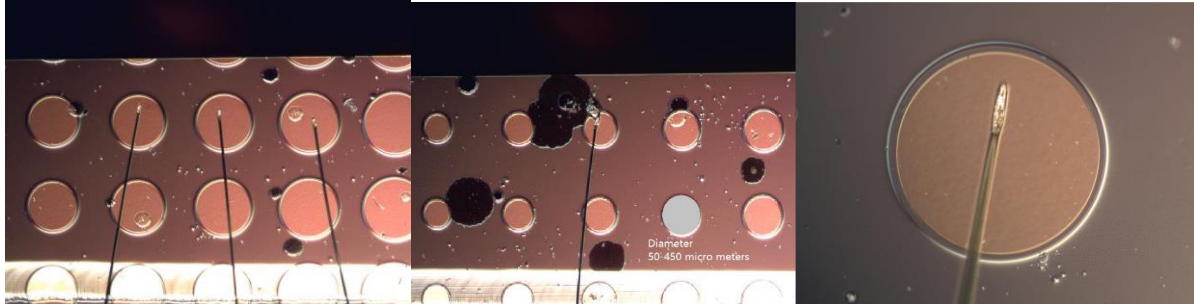
Figure 4.6: Microscopic photos of the disk shaped mid-infrared quantum cascade lasers. The diameters of the disks change from 50 to 450 μm.

As shown in the microscopic picture in Figure 4.6, the disk electrodes and waveguide of the mid-infrared quantum cascade lasers are fabricated in different in sizes. The diameters of the disks are designed in the ranges of 250 μm to 430 μm. The top electrode on the devices and the outer circuit are connected with 15-μm-wide gold wires using a wire bonding machine (K&S 4523). There are a number of devices on every single piece of wafer. Before the testing, a probe station is used to roughly measure the electrical features. By gently touching the electrodes with a probe, the resistance of the device can be measured under a low bias voltage (~0.8 V), as shown in Figure 4.7. The quality of the fabrication and wafer growth is unevenly spatial. The results of the probe station measurement fundamentally show the properties of the device. Considering the resistance of each device, a selection can be made among the large number of devices. The devices with extremely low or high resistance are eliminated in this first step of measurement.
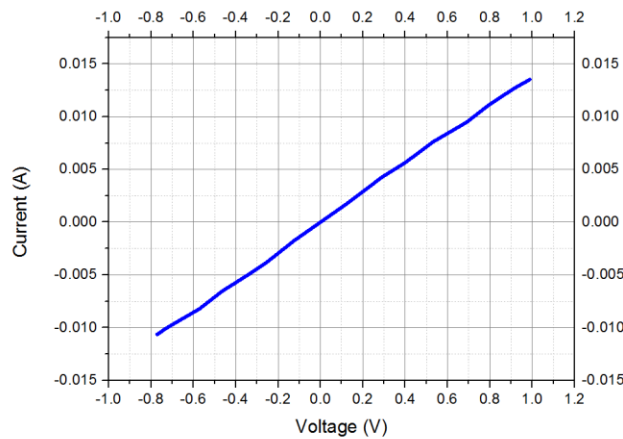
Figure 4.7: Results of the probe station measurement. ±0.8 V voltage is applied to the devices through the probes. The current-voltage curves provide information about the electrical properties.

After wire bonding, the devices are sent to the light-current-voltage (LIV) measurement system in the lab. Shown in Figure 3.1 and 4.8.
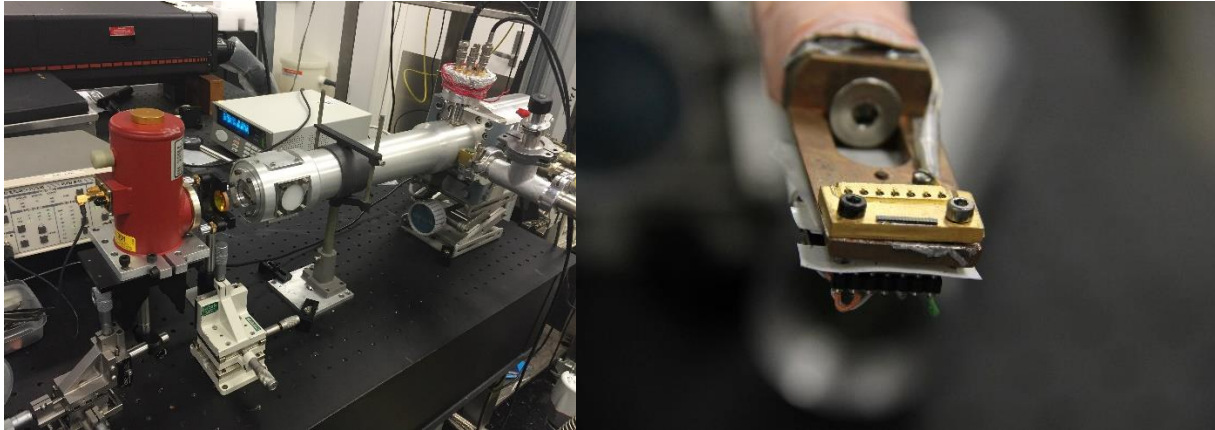
Figure 4.8: Photos of the light-current-voltage measurement system in our lab.

The LIV feature at different temperature is measured with the measurement system, which is shown in Figure 3.1 and Figure 4.8. In the first few series of the mid-infrared quantum cascade lasers, the density of defects is rather high, and the quality of the fabrication is not good. As a result, the current-voltage curves are unexpected as shown in Figure 4.9(a). The laser device is burned at low bias voltage (<10V). Beyond the burning point, some parts of the quantum structure are destroyed. The burned MIR QCLs show IV features such as shorted circuit (large current under low voltage).

A small number of MIR QCLs from the first generation show reasonable current-voltage curves, like in Figure 4.9(b). However, no radiation were detected from those devices. It is possible that the light from the devices is non-directional and too weak to be detected. Generally, it is clear that the quality of the first generation of disk devices (from wafer G0144) needs to be improved.
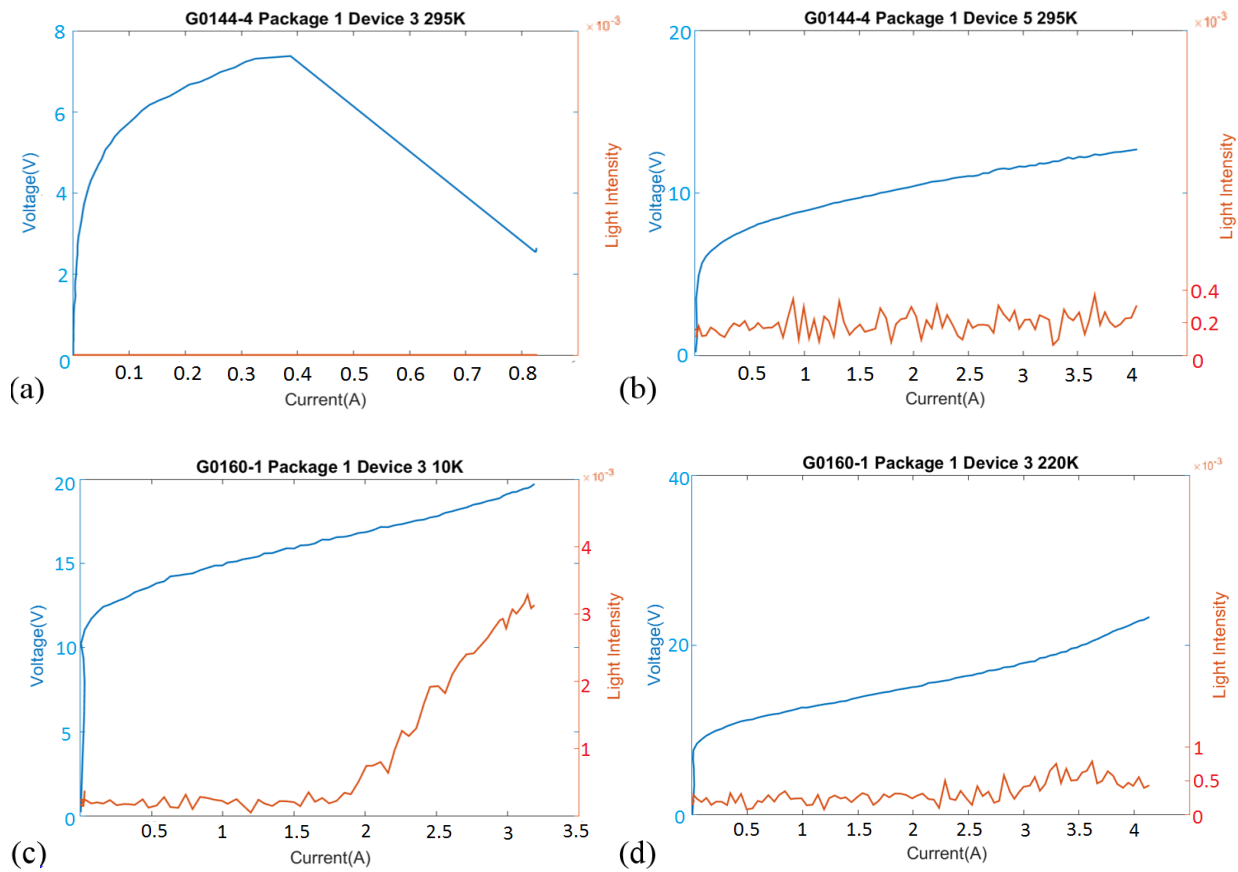
Frequency	Pulse Width	Device Diameter
1 kHz	250 ns	G0144-4 370.6 μm/device 3 271.3 μm/device 5 G0160-1 407.7 μm

Figure 4.9: Light-current-voltage curves of the G0160 disk shaped mid-infrared quantum cascade lasers. The blue lines are the current-voltage curves. The orange lines are the light-current curves.

In the meanwhile, more wafers are grown (G0160, G0162and G0173) and made into disk devices. The first obtained lasing device is from the wafer G0160 (shown in Figure 4.9(c)). This was also the first time a mid-infrared quantum cascade laser is completely made in Waterloo by our group. As expected, the light power from the disk waveguide is too weak. The noise level is fairly high, but the signal of the light intensity and the threshold current can still be seen at a low temperature (10 K). Considering the temperature dependent performance, the light intensity can still be detected at up to 220 K (Figure 4.9(d)).

50
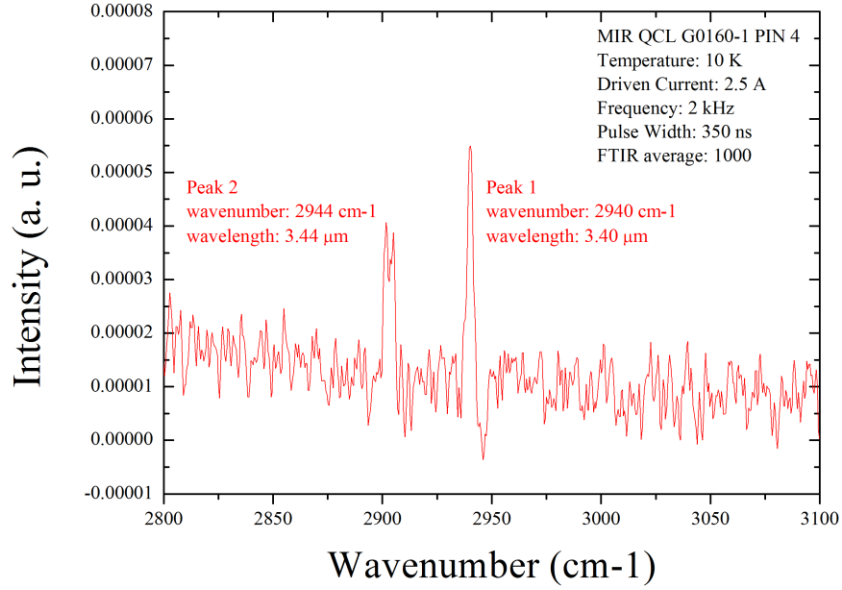
Figure 4.10: Spectrum of the G0160 disk mid-infrared quantum cascade laser. Because of the disk shape, the collected light intensity is weak.
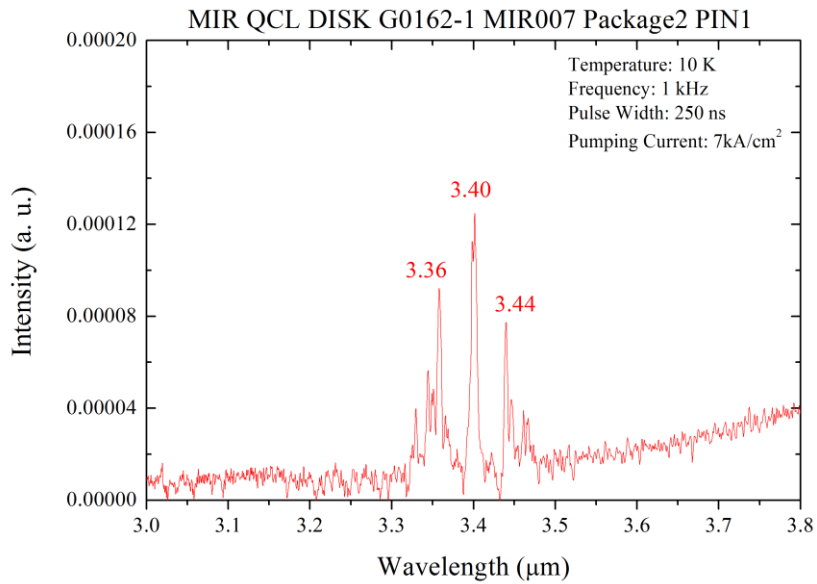
Figure 4.11: Spectrum of the G0162 disk mid-infrared quantum cascade laser. The light intensity is stronger than that of the G0160 lasers.

To further check the device performance, the spectrum measurement is done with a FTIR spectrometer (BRUKER IFS66v/S). The best spectrum out of the G0160 disk devices is shown above in Figure 4.10 and Figure 4.11. The peaks are located at 3.40 and 3.44 μm which is slightly different from the designed value, 3.50 μm. Since the active region of a MIR QCL always has a relatively wider gain spectral range, this result looks reasonable. However, the noise is caused by the weak light intensity. Thus, the ridge devices are believed to have better performance than the disk ones.
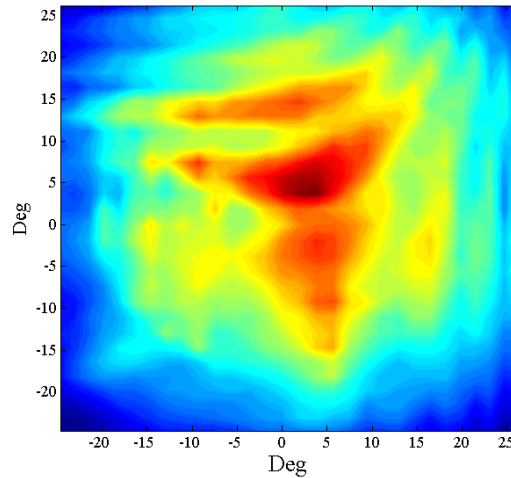
Figure 4.12: Result of the beam pattern measurement for the G0160 disk shaped mid-infrared quantum cascade laser.

The far-field distribution from the G0160 disk devices is shown above in Figure 4.12. The beam pattern is measured at 10 cm ahead of the laser. As can be seen in the figure, the light intensity is mainly distributed within the angle of ±15°. The collimation of this kind of laser is relatively poor because of the shape of the waveguide. The round shape has no selectivity of direction, hence, the light can be caught from different angles.
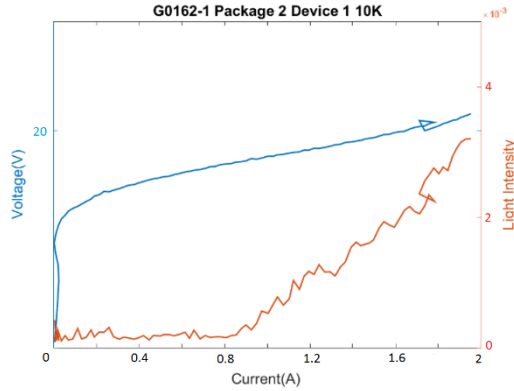
Frequency	Pulse Width	Device Diameter
1 kHz	250 ns	190 μm

Figure 4.13: Light-current-voltage curves of the G0162 disk shaped mid-infrared quantum cascade lasers.

The performance of the MIR QCLs from G0162 wafer is slightly better than those from G0160. From the LIV curves in Figure 4.13, a threshold current density of 3 kA/cm^2 can be clearly seen. Although the light intensity is still low, we can say the mid-infrared quantum cascade lasers was achieved in the University of Waterloo.

The same fabrication processes are also done with wafer G0173, but no light is found. After several repetitions, the growth quality of G0173 is considered to worse than expected.

Wafer G0212 and G0214 are grown for the next step of the research using a ridge waveguide. Before that, several pieces of these two wafer are selected to be fabricated to disks shape for comparison.

As can be seen in the table of the measured disk of the mid-infrared quantum cascade lasers, the success ratio is fairly low. This means the producing techniques require further improvement.

Below is a summary of the measured disk lasers (Table 4.2):

Wafer Number	Piece Number	Package Number	Device Number					
			1	2	3	4	5	6
G0144	①	1		green	green	green	black	black
		2			blue	blue	blue	
	④	1		blue	blue	green	blue	blue
G0160	①	1		blue	blue	yellow	blue	blue
		2	blue	yellow	yellow			blue
G0173	①	1	gray	green	blue	blue		
		2	gray	gray	blue	green		
		3	green	green		blue	green	
		4		green				green
		5	green	blue		blue	blue	
G0162	①	1			blue	blue	blue	green
		2	yellow			blue	black	yellow
G0212	①	1	gray	blue	green	green	green	blue
		2	green	green	green	gray	green	green
		3	gray	blue	green	green	gray	blue
		4	green	blue	green	green	green	gray
		5	green	green	green		green	green

G0214	③	1						
		1		blue	green	gray	blue	green
		2			blue	green	blue	green
		3						
		4	gray	blue	green	green	blue	
		5						
		6	blue	green	green	blue	green	
G0232	①	2	blue	gray	blue	yellow	blue	blue

Short or too low resistance ▰ (gray)

Open or too high resistance ▰ (black)

Burned under low bias ▰ (green)

IV okay without light ▰ (blue)

Lasing at low temperature ▰ (yellow)

Lasing at room temperature ▰ (red)

Table 4.2: Status of the disk shaped mid-infrared quantum cascade lasers.

4.3 Ridge Devices

As a prototype of the mid-infrared quantum cascade lasers, the disk lasers provide information on the quality of the growth and fabrication processes. The characterizing system is also verified while testing the disk mid-infrared quantum cascade lasers. However, the round-shaped waveguide do not provide a good performance of light emission. The light path inside the waveguide is not directional. Thus, the power and collimation of the light are not desirable. Although, after several material growth attempts, the quality of the MBE grown superlattice becomes much better. Therefore the need to obtain better optical performance has resulted in the fabrication of ridge shaped mid-infrared quantum cascade lasers.
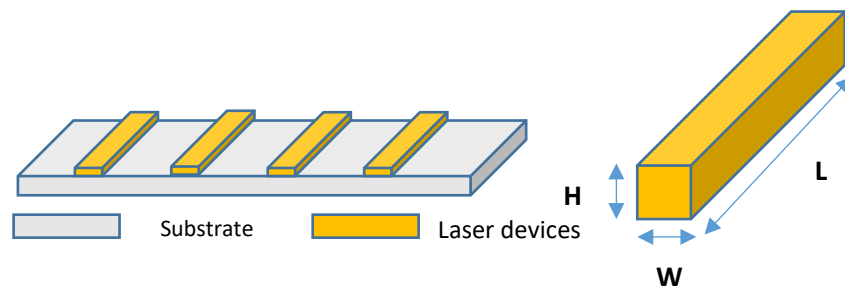
Figure 4.14: 3-D sketch of the fabricated ridge shaped mid-infrared quantum cascade lasers

The size of the ridge waveguide is ~ 10 μm (H) $\times \sim 10$ μm (W) $\times \sim 1\ mm\ (L)$, as shown in Figure 4.14. The widths of the ridges are 9, 11, 12.5, 14 or 16 μm as defined by the mask. Since the top electrode of the device is too narrow (~10 μm), a gold bonding pad is fabricated to expand each electrode. The 100-μm-wide bonding pad makes it easier to connect the device to the outside circuit. The cross section and microscopic photos are shown in Figure 4.15.
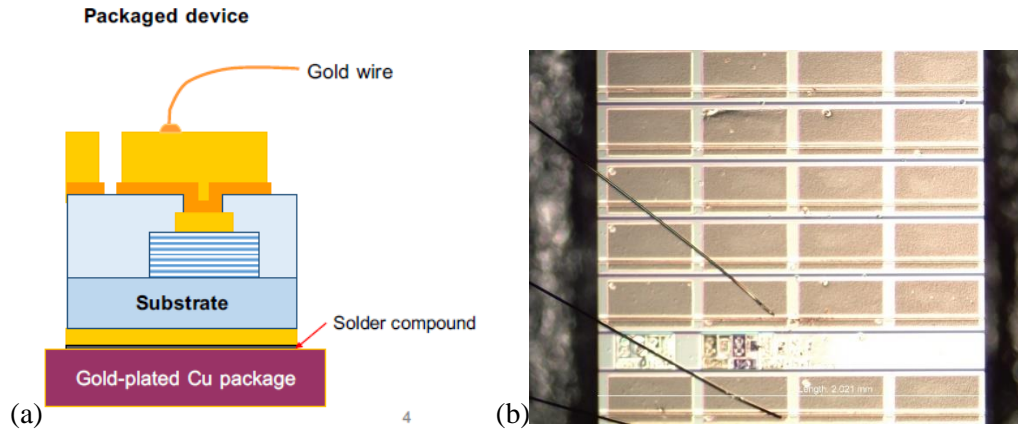
Figure 4.15: (a) Cross section of ridge shaped MIR QCLs. (b) Microscopic photo of the top view of ridge shaped MIR QCLs.

4.3.1 3.5 μm Wavelength Mid-infrared Quantum Cascade Lasers

Because the first working laser in this project is from wafer G0160, this wafer is selected to be the material for the first ridge device. After measuring the G0160 ridge devices, the electrical properties of most of the devices are found to be problematic, either short or open circuit. Then a dummy device is sent to scanning electron microscopy (SEM) measurement.
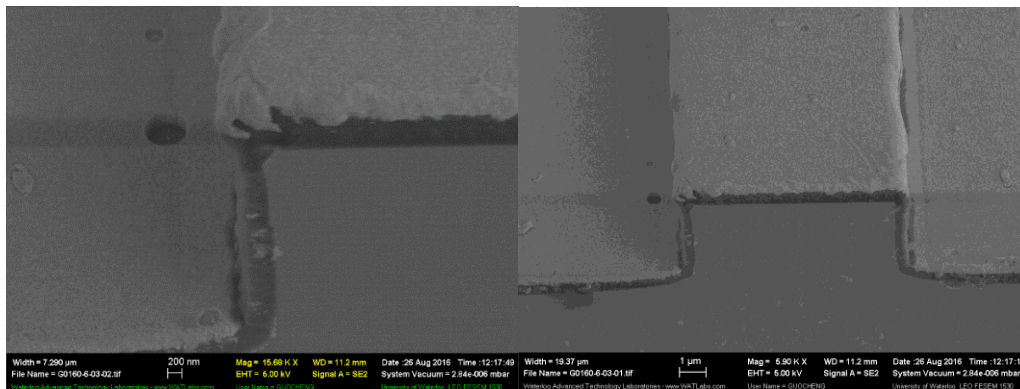
Figure 4.16: Scanning Electron Microscopy photos of the G0160 ridge shaped mid-infrared quantum cascade lasers.

In the proposed design, the gold layer is supposed to cover the whole top surface around the ridge waveguides. In the SEM images in Figure 4.16, the top light-colored layer is the electrode material. It seems that the gold layer is rough in thickness, and the side walls of the ridge waveguide are not fully covered. The darker colored layer is supposed to be SiN. This insulating layer looks smooth and uniform. Thus, the reason for the failure of these G0160 ridge devices might be due to the quality of the side wall gold layer, which is a structure that does not exist in the previous disk devices.

After several attempts, the devices with the best performances are fabricated from the wafer pieces of G0232-10 and G0233-7.
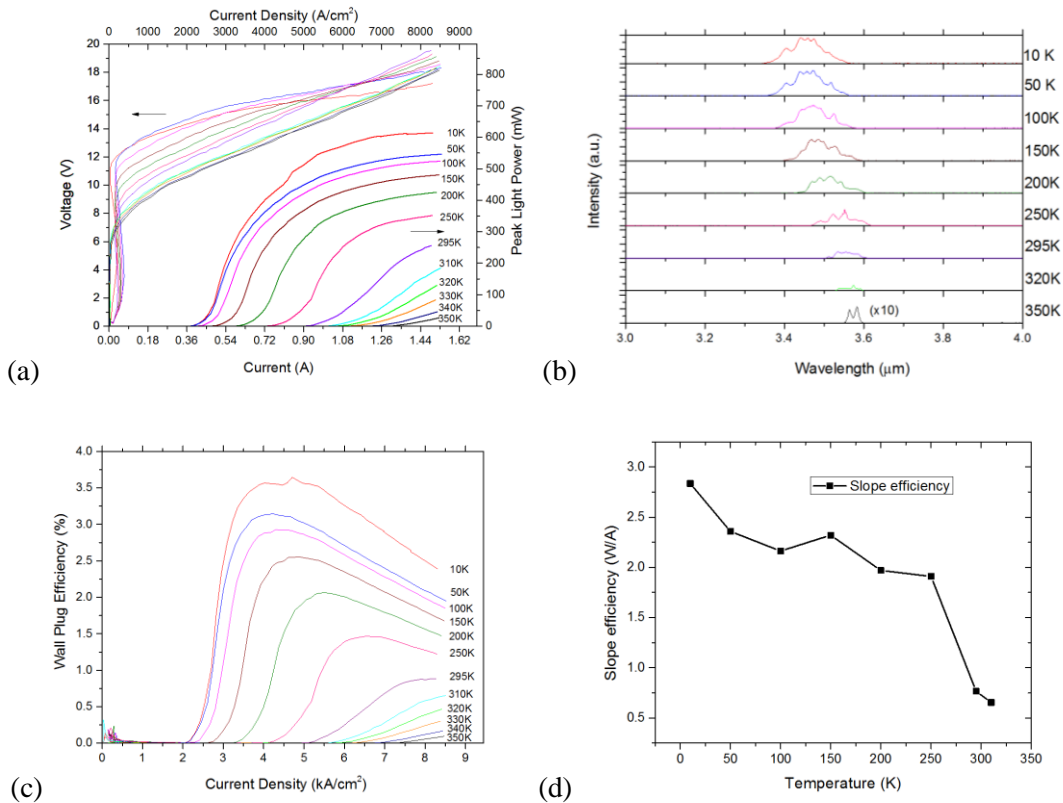
Figure 4.17: Characterization results of the G0233-7 laser. All the results are measured at different temperatures (10-350 K) (a) Light-current-voltage.(b) Spectrum. (c) Wall plug efficiency (light power/pumping power). (d) Slope efficiency (light power per unit current).

The light-current-voltage curves, spectrums, and efficiencies at different temperatures are shown in Figure 4.17 [15]. This laser shows strong light power of up to 600 mW in pulse. And the emission light can be detected at up to 350 K, which is the highest temperature in our setup. The spectrum also shows a reasonable shape. The center wavelength shifts from 3.45 μm to 3.55 μm as the temperature increases. Here, the good performance of the MIR QCLs verifies the quality of the growth, fabrication and the whole measuring method. Later on, with the 3.5 μm mid-infrared quantum cascade lasers, more knowledge about the mid-infrared quantum cascade lasers were obtained.
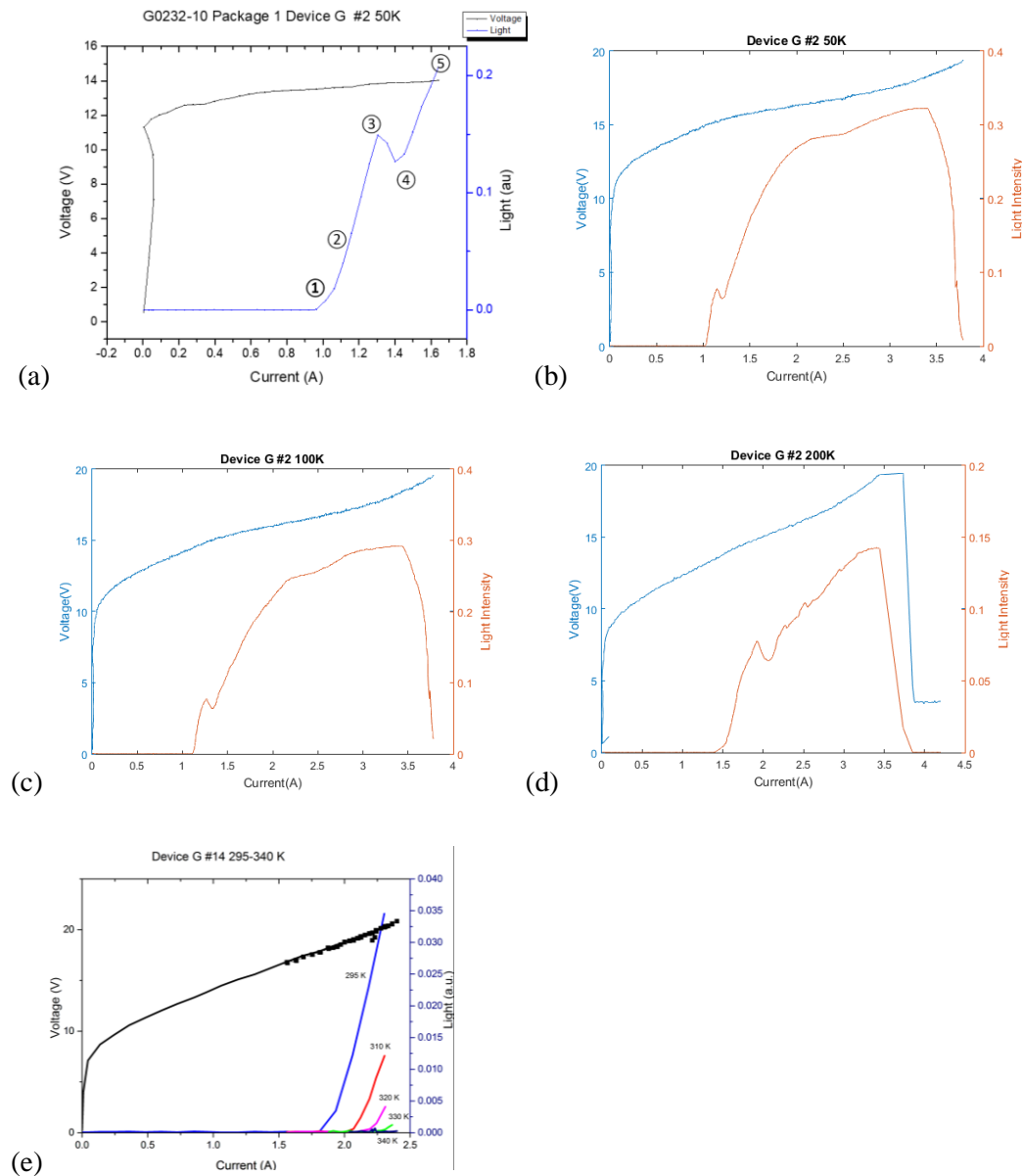
Figure 4.18: Light-current-voltage curves of the G0232-10 device at various temperatures. (a) Zoom-in figure of the sub-peak. (b) 50 K. (c) 100 K. (d) 200 K. (e)Above room temperature.

Using a measured Device G (G0232-10 Package 1), the relationship between the light intensity and current is found to have an interesting feature. Figure 4.18 shows that there are two peaks in the light-current curves.
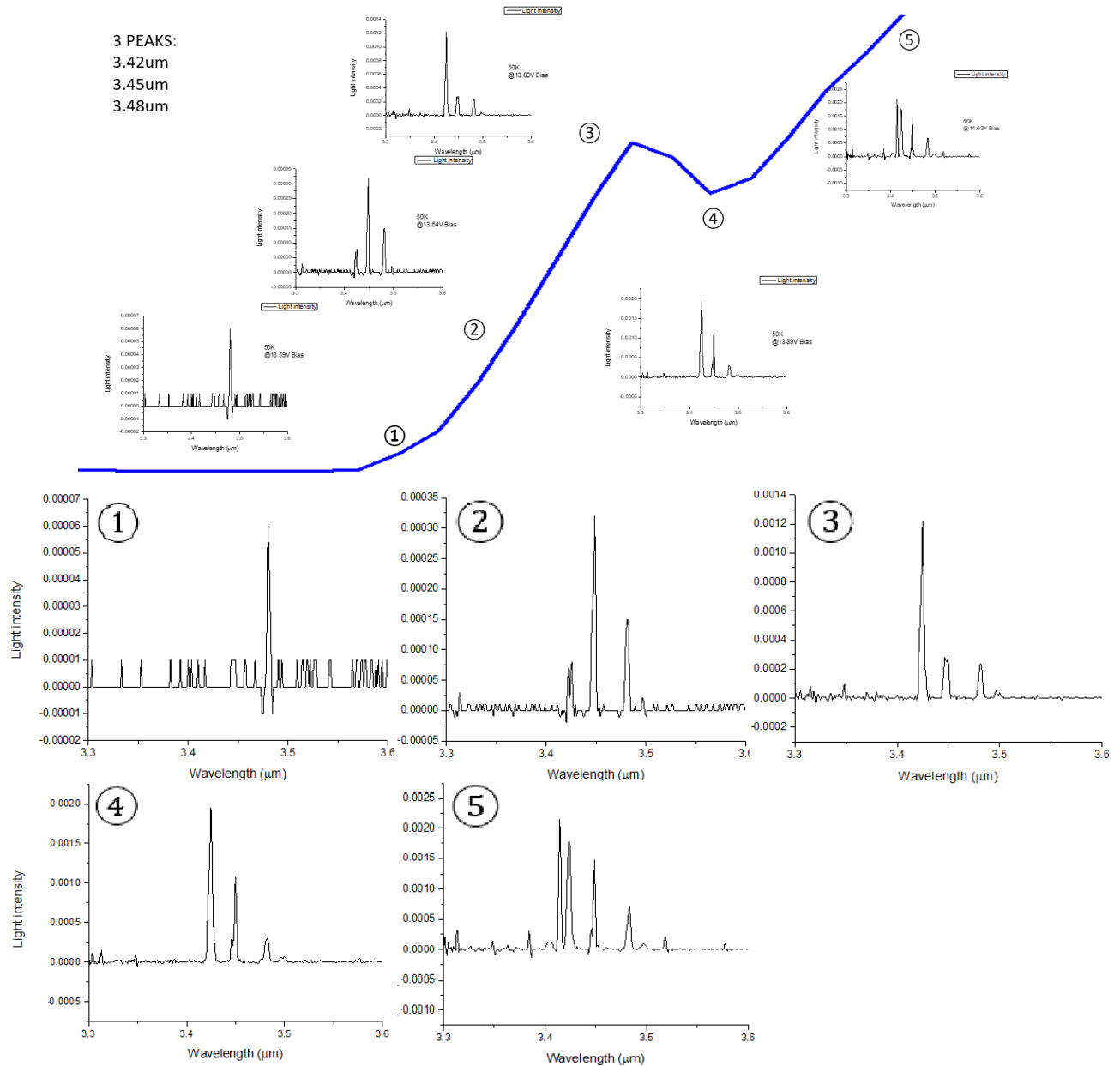
Figure 4.19: Spectrum of the G0232-10 laser with various bias voltage.

To further analyze the performance of the tested lasers, the spectrum is measured under different conditions. The shape of the spectrum changes with an injection of current as shown in Figure 4.19. With alower current, the peak at 3.48 μm is much stronger than the others. As the current increases, however, the 3.42 and 3.45 μm grow faster and become higher than the longer wavelength peak.
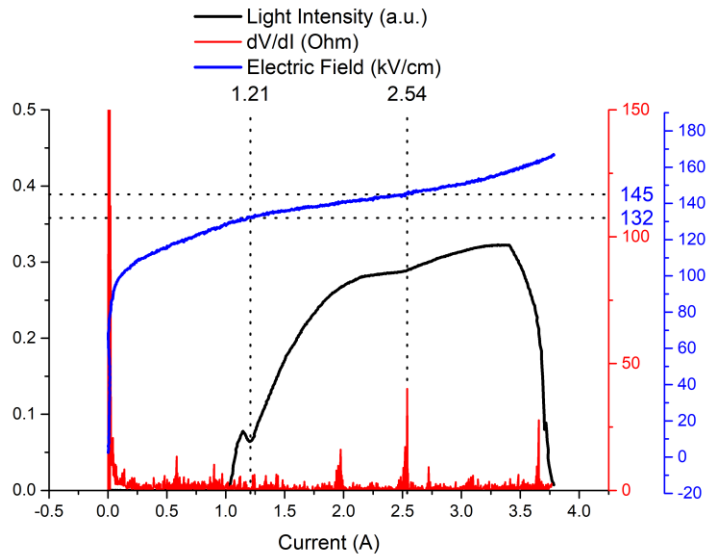
Figure 4.20: Light-current-voltage-differential resistance feature of G0232-10 #2 at 50K.

Additional information is from the differential resistance. The differential resistance (dV/dI) plotted in Figure 4.20 shows the relationship between the light intensity and the inner quantum structure. The peaks of differential resistance, which is the points with ineffecient current transition, is believed to be the reasons for reduction of the light intensity.

The simulation about the electron transiton is done to describe this phenomenon.
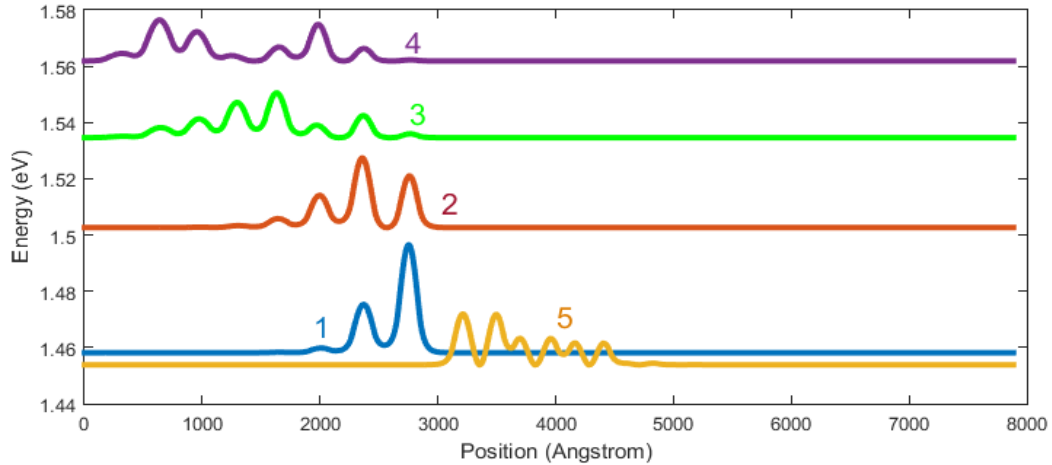
Figure 4.21: Wave function of the upper lasing state and the nearest states in the injection section.
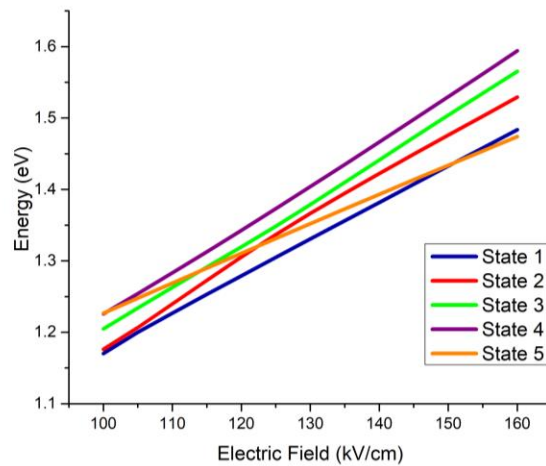
Figure 4.22: The relative energies of the upper lasing state (State 5) and the four lowest states (State 1 to 4) of the injection section.

Figure 4.21 shows the wave functions of the upper lasing state (State 5) and the four closest states (States 1 to 4) in the injection section. All the carriers in State 5 can be assumed to be injected from these four states. The relative energy positions of these five states are shown in Figure 4.22. As can be seen in the figure, with lower bias voltage (<100 kV/cm), the upper lasing state (State 5) become higher than the other state in the figure (States 1 to 4). The upper lasing state become relatively lower and lower as the bias voltage is increased. Based on the mechanism of the carrier transport, the transition rate for the tunnelling and most of the scatterings normally become strengthened as the energy difference draw close to zero. One exception is the LO phonon scattering, which is enhanced with the energy difference equal to the phonon energy (~30 meV in InAs).
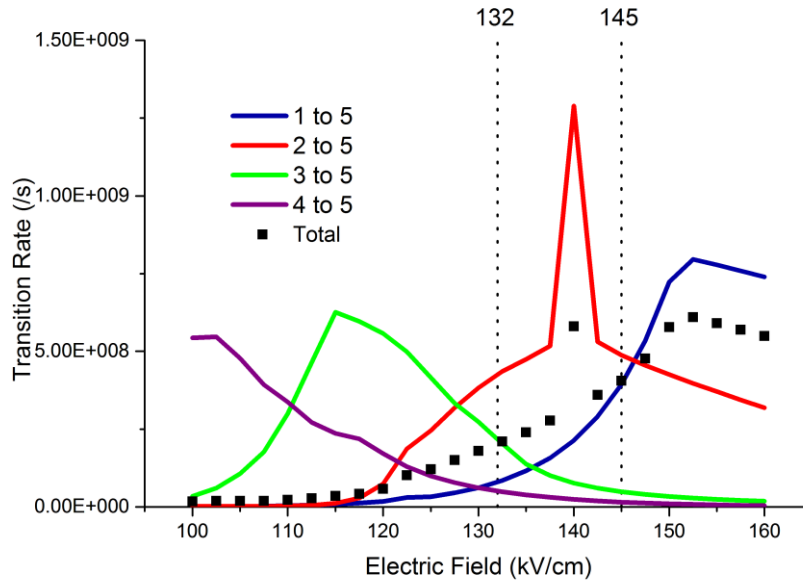
Figure 4.23: Transition rate from the injection states to the upper lasing state.

Figure 4.23 shows the injection rate to the upper lasing state based on the energy structure discussed above. The transition rate at the highlighted location is relatively lower and corresponds to weaker light power.
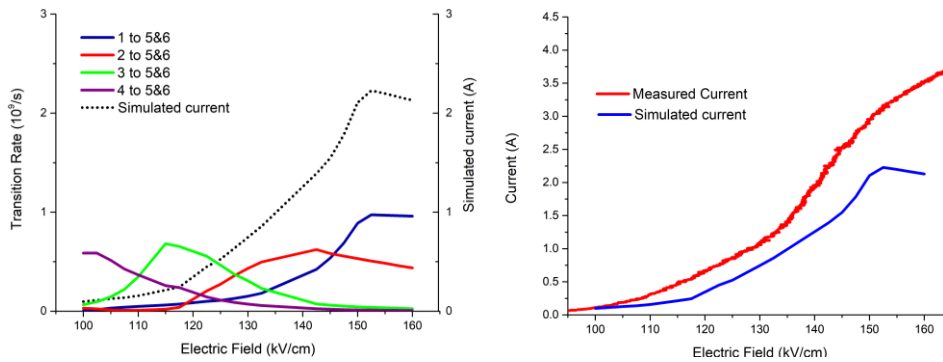
Figure 4.24: Simulation results of transition rate and current-voltage curve for G0232 at 50K.

To finalize the simulation results, the simulated current-voltage curve is plotted as shown in Figure 4.24. The assumption added here is that all the carriers injected to the active region pass through state 5 and the nearest state above it (states). Thus, some other paths are ignored in the simulation, and, as a result, the current is slightly lower than the empirical value.
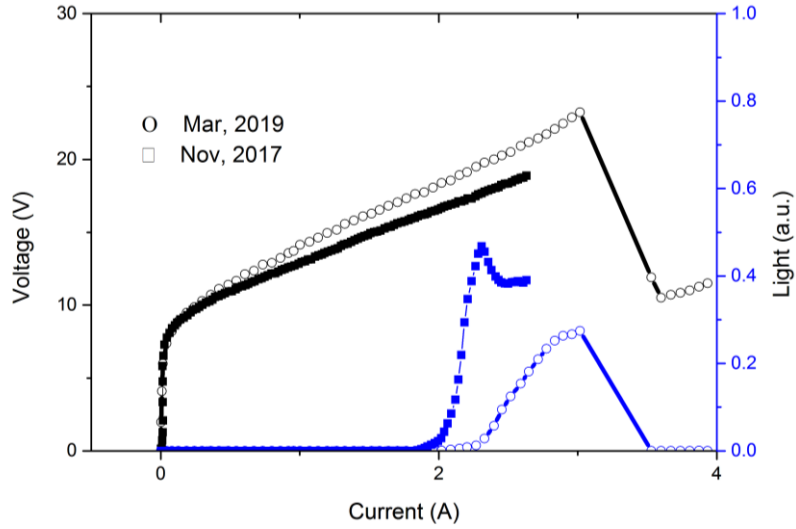
Figure 4.25: Current-light-voltage measurement result for the same device (G0232-10 #7) at different date (Mar 2019 and Nov 2017).

Another effect that should be considered is the durability of the mid-infrared quantum cascade devices. For a single laser device, the performance was measured twice at different dates. From Figure 4.25, the performance of the laser was greatly reduced. Even though the laser was stored in a nitrogen gas purged dry box during this period, there was still damage or contamination of the device. According to the electrical performance, one possible explanation is the oxidization. The unpredictable oxidized areas form additional resistors in the circuit, and the unstable structure of the oxidized parts bring in more risks of device burning.

Table 4.3 is the summary of the 3.5 μm ridge lasers

Wafer Number	Piece Number	Package Number	Device Number															
			1	2	3	4	5	6	7	8	9	10	11	12	13	14	15
			1			2			3			4			5			6
G0160	②	1																
		2																

Group	No.	Row						
	⑤	1	blue	blue	blue	black	black	blue
		2	green	black	green	black	white	green
		3	gray	green	black	black	black	black
G0214	①	1	gray	gray	gray	gray	gray	gray
		1R	white	white	white	white	gray	white
	②	1	green	green	gray	red	gray	gray
		1R	white	white	gray	white	gray	red
		2	green	green	gray	gray	gray	yellow
		3	white	blue	red	black	yellow	green
G0212	②	1	gray	gray	green	white	yellow	blue
		2	green	white	green	red	red	white
	③	1	black	black	black	black	white	black
		1R	white	black	black	gray	white	white
G0232	②	1	gray	green	green	gray	green	white
	③	1	green	green	green	green	gray	green
	⑥	1	gray	gray	red	gray	gray	gray
	⑦	1	gray	yellow	yellow	gray	gray	gray
		2	gray	gray	gray	gray	gray	white	white	white	white	white	white	white
		3	gray	gray	white	white	white	white	red	white	white	white	white	white
	⑩	1	gray	red	gray	green	gray	red	red	yellow	green	green	green	white	gray	red	gray

G0233																	
	①	1	white	green	green	green	green	green									
		2	gray	green	gray	gray	gray	gray									
		2R	gray	white	gray	white	gray	gray									
	②	1	gray	green	gray	green	gray	gray									
		3	white	red	green	green	green	yellow									
	⑦	1	red	red	gray	red	white	gray									
		2	gray	gray	gray	gray	green	green	green	green	gray	red	green	red	gray	red	gray
		3	red	red	red	gray	red	red	gray	red	red	red	red	green	gray	gray	gray
	⑪	1	white	white	white	white	white	white	white	white	white	blue	white	white	red	white	

Legend:

- ▢ (gray) Short or too low resistance
- ▮ (black) Open or too high resistance
- ▢ (green) Burned under low bias
- ▢ (blue) IV okay without light
- ▢ (yellow) Lasing at low temperature
- ▢ (red) Lasing at room temperature

Table 4.3: Status of the ridge shaped 3.5 µm mid-infrared quantum cascade lasers.

4.3.2 9 μm Wavelength Mid-infrared Quantum Cascade Lasers

Longer wavelength (~9 μm) mid-infrared quantum cascade lasers are fabricated using the same method for the 3.5 μm lasers. The size of the devices is almost the same, ~ 10 μm (H) $\times \sim 10$ μm (W) $\times \sim 1\ mm\ (L)$. The photos of the packages are shown in Figure 4.26. The wafer G0241 is based on the design from H. Page [13]. This GaAs/Al$_{0.45}$Ga$_{0.55}$As based MIR QCL was reported to operate at room temperature with a radiation of ~9 μm light. The performance of the GaAs based lasers in this work is not perfect as predicted.
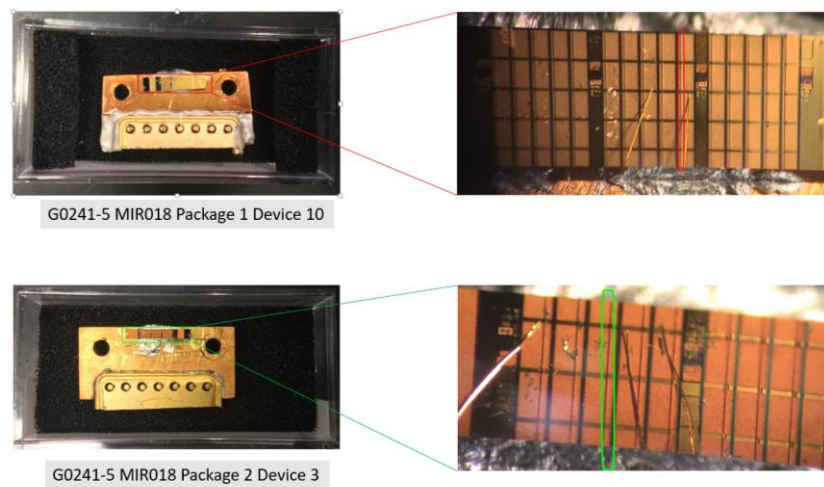
Figure 4.26: Photos of G0241 9 μm ridge shaped mid-infrared quantum cascade lasers.
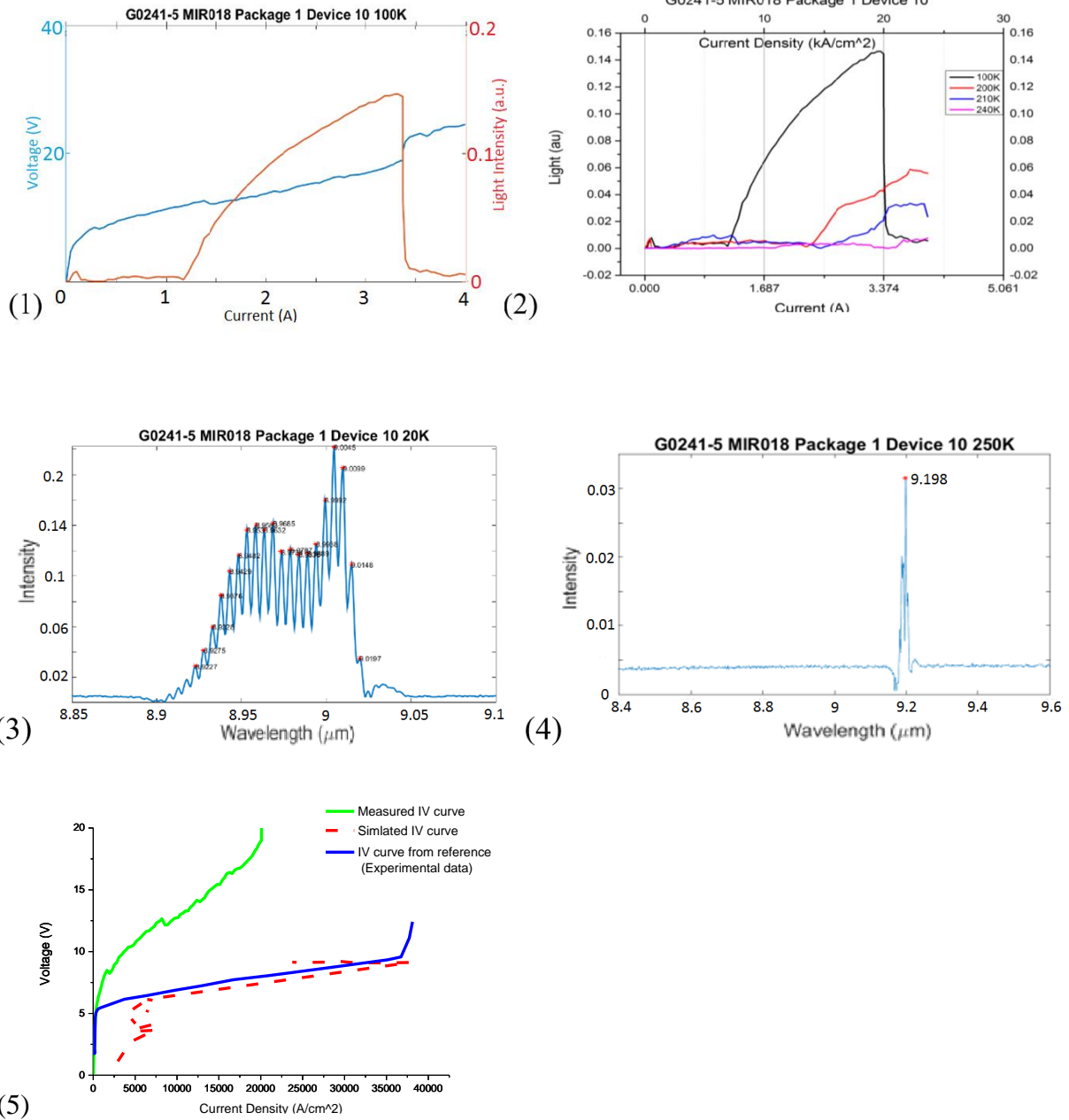
Figure 4.27: (1)(2) Light-current-voltage curves of the G0241 9 μm ridge shaped mid-infrared lasers. (3)(4) Spectrum of the G0241 device. (5) Comparison of the experimental and theoretical IV curves.

As shown in Figure 4.27 (5), the measured voltage is relatively higher than the theoretical prediction. There might be two reasons: First, the conduction inside and outside the device is not perfect, therefore, some resistances exist in the circuit. Second. the effective surface area is smaller than expected, which means the current density was underestimated.

The GaAs based 9 μm mid-infrared quantum cascade lasers are measured at different temperatures. At up to 250 K, light can still be detected from the devices. The spectrum results clearly show the Fabry-Perot modes. The free spectrum range measured is 0.0051 μm, which is very close to the theoretical value of 0.0050 μm.

Table 4.4 is the summary of the 9 μm ridge lasers

Wafer Number	Piece Number	Package Number	Device Number														
			1	2	3	4	5	6	7	8	9	10	11	12	13	14	15
			1		2			3			4			5			6	
G0241	①	1	green	blue	gray	gray	blue	gray	gray	gray	gray	gray					
	③	1	black	black	black	black	black	gray	gray	black	black	black	black	black	black	black	black
	④	1		blue									yellow	yellow	yellow	yellow	yellow
	⑤	1		blue	yellow	blue	blue	yellow	yellow	yellow	yellow	yellow					
		2	blue	yellow	yellow	yellow	yellow										

Short or too low resistance — gray

Open or too high resistance — black

Burned under low bias — green

IV okay without light — blue

Lasing at low temperature — yellow

Lasing at room temperature — red

Table 4.4: Status of the ridge shaped 9 μm mid-infrared quantum cascade lasers.

4.4 Summary

The setups for all the measurement reported in this Chapter are introduced in Chapter 3. With the help of the selected measurement systems, the mid-infrared quantum cascade lasers are characterized in multiple ways. As reported in the experimental results on this chapter, IV, spectrum, XRD, SEM, and beam pattern measurements were performed for most or some of the laser devices. Valuable data about the devices can be obtained from these measurements.

In this chapter, the characterization process of the mid-infrared quantum cascade lasers is demonstrated. A number of spectrum and IV measurement results provide information about the laser devices. Among all the mid-infrared quantum cascade lasers made and measured at the University of Waterloo, the 3.5 μm wavelength InAs/AlSb based lasers demonstrated the best temperature performance. The highest operating temperature is up to 350 K (based on the measurement setup). Based on simulated results, the characteristic optical performance of the G0232 lasers can be explained with the effect of inefficient carrier injection. From the present results, the maximum operating temperature for the 9 μm wavelength GaAs/AlGaAs based lasers is around 250K, which is lower than the expected. According to the reference [13] and the theoretical analysis reviewed in Chapter 2, this GaAs based design is expected to work at room temperature, but, defects from the growth and fabrication or improper operations could hinder this result. More repeated rounds are needed to verify the problem.

Chapter 5

Conclusion and Discussion

5.1 Conclusion

As a promising light source for mid- to far- infrared radiation, quantum cascade lasers show potential for application in multiple fields, such as gas sensing and chemical analysis. To a certain extent, intersubband transition based semiconductor devices, such as mid-infrared quantum cascade lasers, are independent of band gaps and material types. These mid-infrared quantum cascade lasers provide a larger space for engineering and designing. Furthermore, the performance of these mid-infrared quantum cascade lasers greatly depends on the accuracy of the quantum design, quality of material growth and fabrication.

In Chapter 2, the theoretical analysis was introduced and verified. The computer program in this work used a self-developed code based on the combination of the transfer matrix and the rate equation methods. The electrical and optical performance of the mid-infrared quantum cascade lasers can be predicted by the simulation results. For the AlGaAs/GaAs lasers, one aim was to push the original design [13]to longer wavelength (9.5 µm) to satisfy the application of detection of chemicals, such as alcohol. The simulation program was a convenient method to modify the quantum structure. The results obtained from simulation program which are discussed in Chapter 2 demonstrated that the process is reliable. However, the simulation method is still being developed, and strategies to improve the mid-infrared quantum cascade laser simulation are being studied by the researchers. Faster and more accurate software is always attractive in this field.

In Chapter 3 and Chapter 4, the measurement setup and results were reported. The experimental setups for the mid-infrared quantum cascade lasers were specified. In this work, the experiments were completed from low temperature (10 K) to high temperature (350 K), low pressure (10^{-5} mTorr) to high pressure (atm), and under various electrical conditions. The laser devices were fully characterized in the lab. The theoretical results were also verified by the performance of the mid-infrared quantum cascade lasers.

This thesis presents two types of mid-infrared quantum cascade lasers, a 3.5 µm wavelength based on InAs/AlSb and a 9 µm wavelength based on AlGaAs/GaAs. All processes were completed at the University of Waterloo. With the step by step improvements in the techniques, the above room temperature operation for the 3.5 µm devices was achieved in pulse mode with the peak power of hundreds of milliwatts. Also, a proper explanation is discussed about the kinks of light intensity. The highest operating temperature of the 9 µm lasers is around 250 K. Additionally the simulation methods, fabrication and characterization technologies were developed.

5.2 Future Works

The presented AlGaAs/GaAs based mid-infrared quantum cascade lasers demonstrated good performances at low temperatures (<200 K). However, the light intensity rapidly decreases at higher temperature, and as a result, the highest operating temperature limit is 250 K. The wafer used for these mid-infrared quantum cascade lasers had an error of 3% in the thickness of layers, and, the fabrication processes were not ideal. To achieve higher operating temperature, more repetition will be needed. Hopefully, with the high quality material growth and fabrication, the temperature performance of the AlGaAs/GaAs mid-infrared quantum cascade lasers can be improved.

Another direction for the future work is to achieve a quasi DC or DC operation with both AlGaAs/GaAs and AlAs/InSb lasers. Thermal dissipation is the main challenge for the continuous wave pumping. A buried active core might be a possible method to improve the thermal conduction [27].

Some techniques have been developed to further expand the application of the mid-infrared quantum cascade lasers. For example, an external cavity [28] or gratings [29]could be integrated with the presented lasers to provide more functions.

.

References

[1] J. Faist, Quantum cascade lasers, Oxford: Oxford University Press, 2013.

[2] P. Werle, F. Slemr, K. Maurer, R. Kormann, R. Mucke and B. Janker, "Near and mid-infrared laser optical sensors for gas analysis," *Opticas and Lasers in Engineering,* vol. 37, no. 2-3, pp. 101-114, 2002.

[3] S. G. Razavipour, "Design, Analysis, and Characterization of Indirectly-pumped Terahertz Quantum Cascade Lasers," *University of Waterloo, Ph. D thesis,* 2013.

[4] A. Elia, P. M. Lugara, C. D. Franco and V. Spagnolo, "Photoacoustic Techniques for Trace Gas Sensing Based on Semiconductor Laser Sources," *Sensors,* vol. 9, no. 12, pp. 9616-9628, 2009.

[5] J. Faist, F. Capasso, D. L. Sivco, C. Sirtori, A. L. Hutchinson and A. Y. Cho, "Quantum cascade laser," *Science,* vol. 264, no. 5158, pp. 553-556, 1994.

[6] M. S. Vitiello, G. Scalari, B. Williams and P. D. Natale, "Quantum cascae lasers: 20 years of challenges," *Optics Express,* vol. 23, no. 4, pp. 5167-5182, 2015.

[7] B. Bozok, "Mid-infrared Quantum Cascade Laser," *Bilkent University Mater Thesis.*

[8] N. Bandyopadhyay, Y. Bai, S. Silvken and M. Razeghi, "High power operation of $\lambda \sim 5.2$–11 µm strain balanced quantum cascade lasers based on the same material composition," *Appl. Phys. Lett,* vol. 105, no. 7, 2014.

[9] M. S. Vitiello and G. Scamarcio, "Subband electronic temperatures and electron-lattice energy relaxation in terahertz quantum cascade lasers with different conduction band offsets," *Appl. Phys. Lett,* vol. 89, no. 13, 2006.

[10] M. Nobile, P. Klang, E. Mujagic, H. Detz, A. M. Andrews, W. Schrenk and G. Strasser, "Quantum cascade laser utilising aluminium-free material system: InGaAs/GaAsSb lattice-matched to InP," *Electronics Lettes,* vol. 45, no. 20, pp. 1031-1033, 2009.

[11] M. Bahriz, G. Lollia, P. Laffaille, A. N. Baranov and R. Teisser, "InAs/AlSb quantum cascade lasers operating near 20 μm," *Electronics Letters,* vol. 49, no. 19, pp. 1238-1240, 2013.

[12] Z. R. Wasilewski, M. M. Dion, D. J. Lockwood, P. Poole, R. W. Streater and A. J. SpringThorpe, "Composition of AlGaAs," *Journal of Applied Physics,* vol. 81, no. 4, p. 1683, 1997.

[13] H. Page, C. Becker, A. Robertson, G. Glastre, V. Ortiz and C. Sirtori, "300 K operation of a GaAs-based quantum-cascade laser at λ≈9 μm," *Appl. Phys. Lett,* vol. 78, no. 22, 2001.

[14] ioffe, [Online]. Available: http://www.ioffe.ru/SVA/NSM/Semicond/AlGaAs/bandstr.html.

[15] X. He, S. Wang, S. G. Razavipour, G. Liu, C. Xu, B. Wen, A. Mahmud, D. Gosselink and e. al, "Characterization for mid-infrared quantum cascade lasers operating up to 350 K on pulse mode," in *CSSTC*, Waterloo, 2017.

[16] S. L. Chuang, Physics of Photonic Devices, WILEY, 2009.

[17] C. Sirtori, F. Capasso, J. Faist and S. Scandolo, "Nonparabolicity and a sum rule associated with bound-to-bound and bound-to-continuum intersubband transitions in quantum wells," *Phys. Rev. B,* vol. 50, no. 12-15, 1994.

[18] S. Rudin and T. Reinecke, "Electron-LO-phonon scattering rates in seminconductor quantum wells," *Phys. Rev. B,* vol. 41, no. 11-15, p. 7713.

[19] H. Sakaki, T. Noda, K. Hirakawa, M. Tanaka and T. Matsusue, "Interface roughness scattering in GaAs/AlAs quantum wells," vol. 51, no. 23, 1987.

[20] R. L. Terrazzi, "Transport in quantum cascade alsers," *ETH Zurich Ph.D Thesis.*

[21] T. Unuma, M. Yoshita, T. Noda, H. Sakaki and H. Akiyama, "Intersubband absorption linewidth in GaAs quantum wells due to scattering by interface roughness, phonons, alloy disorder, and impurities," *Journal of Applied Physics,* vol. 93, no. 3, 2003.

[22] P. Harrison, Quantum Wells, Wires and Dots, John Wiley & Sons, 2016.

[23] E. Dupont, S. F. Z. R. Wasilewski, G. Aers, S. R. Laframboise, M. Lindskog, S. G. Razavipour, A. Wacker, D. Ban and H. C. Liu, "A phonon scattering assisted injection and extraction based terahertz quantum cascade laser," *Journal of Applied Physics,* p. 111, 2012.

[24] M. F. Millea, M. McColl and C. A. Mead, "Schottky Barriers on GaAs," *Phys. Rev,* vol. 177, no. 3, 1969.

[25] T. J. Technologies, "http://www.teledynejudson.com/," [Online].

[26] PIKE Technologies, [Online]. Available: http://www.piketech.com/skin/fashion_mosaic_blue/application-pdfs/CrystalChoiceForTransmission.pdf.

[27] A. Evans, J. S. Yu, J. David, L. Doris, K. Mi, S. Slivken and M. Razeghi, "High-temperature, high-power, continuous-wave operation of buried heterostructure quantum-cascade lasers," *Applied Physic Letters,* vol. 84, no. 3, 2004.

[28] A. Hugi, R. Terazzi, Y. Bonetti, A. Wittmann, M. Fischer, M. Beck, J. Faist and E. Gini, "External cavity quantum cascade laser tunable from 7.6 to 11.4 μm," *Applied Physics Letters,* vol. 96, no. 6, 2009.

[29] B. S. W. Q. Q. A. M. L. Q. H. a. J. L. R. Sushil Kumar, "Surface-emitting distributed feedback terahertz quantum-cascade lasers in metal-metal waveguides," *Optics Express,* vol. 15, no. 1, 2007.